TREM1^{+} regulatory myeloid cells expand in steatohepatitis-HCC and associate with poor prognosis and therapeutic resistance to immune checkpoint blockade

Julie Giraud[1,*], Domitille Chalopin[1,*], Eloïse Ramel[1], Thomas Boyer[1], Atika Zouine[1], Marie-Alix Derieppe[2], Nicolas Larmonier[1], Olivier Adotevi[3], Brigitte Le Bail[4], Jean-Frédéric Blanc[5], Laurence Chiche[5], Macha Nikolski[6] and Maya Saleh[1,7,¶]

[1]University of Bordeaux, CNRS, ImmunoConcEpT, UMR 5164, 33000 Bordeaux, France
[2]University of Bordeaux Animal facilities, 33600 Pessac, France.
[3]Université Bourgogne Franche-Comté, INSERM, UMR1098, 25000 Besançon, France
[4]University of Bordeaux Hospital, Division of Pathology, Pellegrin Hospital, 33000 Bordeaux, France
[5]University of Bordeaux Hospital, Division of Gastrohepatology and Oncology, Haut Leveque Hospital, 33604 Pessac, France
[6]University of Bordeaux, CNRS, IBGC, UMR 5095, 33000 Bordeaux, France
[7]Adjunct Professor, Department of Medicine, McGill University, Montreal, Qc, Canada

*Equal contributions
¶Corresponding author: maya.saleh@mac.com

Keywords: Hepatocellular carcinoma, steatohepatitis, innate immunity, neutrophil-like monocytes, TREM1, immunotherapy.

34 **HIGHLIGHTS:**

35

36 - Atlas of hepatic innate immune cells (100,000 transcriptomes) from patients with HCC
37 - Core signatures to identify, discriminate and localize innate lymphoid and myeloid cells
38 - A population of TREM1^{+}CD163^{+} myeloid cells, referred to as TREM1^{+}CD163^{+} M_{reg},
39 expands in steatohepatitis HCC
40 - TREM1^{+}CD163^{+} M_{reg} express granulocyte- and macrophage/dendritic cell-lineage genes
41 - TREM1^{+}CD163^{+} M_{reg} potently suppress T cell effector functions, which is potentiated by
42 TREM1 engagement by cognate ligands
43 - TREM1^{+}CD163^{+} M_{reg} produce high levels of TGFβ and populate fibrotic lesions
44 - The density of TREM1^{+}CD163^{+} M_{reg} increases in advanced HCC and associate with poor
45 patient survival
46 - The density of TREM1^{+}CD163^{+} M_{reg} associates with resistance to immune checkpoint
47 blockade in other solid tumors

ABSTRACT

Hepatocellular carcinoma (HCC) is an inflammation-associated cancer arising from viral and non-viral etiologies. Immune checkpoint blockade primarily benefits patients with viral HCC. Expansion of suppressive myeloid cells is a hallmark of chronic inflammation and cancer, but their heterogeneity in HCC is not fully resolved and might underlie immunotherapy resistance in the steatohepatitis setting. Here, we present a high resolution atlas of hepatic innate immune cells from patients with HCC that unravels a steatohepatitis contexture characterized by the emergence of high entropy myeloid cell states and myeloid-biased NK cell differentiation. We identify a discrete population of tumor-infiltrating myeloid cells, predominant in the steatohepatitis setting, that expresses a variety of myeloid lineage-affiliated genes, including granulocyte, macrophage and dendritic cell features, and can be identified in HCC tumors based on selective dual expression of *TREM1* and *CD163*. Functional characterization reveals that TREM1^{+} CD163^{+} myeloid cells highly express TGFβ and IL-13RA, localize to HCC fibrotic lesions, and potently suppress T cell effector functions *ex vivo*, a function further potentiated by TREM1 engagement. We refer to this population as TREM1^{+} CD163^{+} regulatory myeloid cells (TREM1^{+}CD163^{+} M_{reg}). Deconvolution analyses in large cohorts of patients with HCC and other solid tumors reveals that the density of TREM1^{+} CD163^{+} M_{reg} increases in advanced stages, associates with poor prognosis, and therapeutic resistance to PD-1 blockade. Our data support myeloid subset-targeted immunotherapies to treat HCC and identify TREM1 as a therapeutic target.

INTRODUCTION

Hepatocellular carcinoma (HCC) ranks among the most common malignancies worldwide, with a rising incidence in the Western World. Despite well-known risk factors, i.e. chronic viral infection with hepatitis B virus (HBV) primarily in Asia and HCV in western countries, excessive alcohol consumption and the metabolic syndrome-associated non-alcoholic steatohepatitis (NASH), HCC is diagnosed late in most patients (Llovet et al., 2021). While several systemic treatment options have been approved for advanced HCC, e.g., sorafenib and other tyrosine kinase inhibitors, they all provide a small clinical benefit (Finn et al., 2020). The landscape of clinical trials for HCC treatment has recently shifted to the field of immunotherapy. The portfolio of therapeutic options now includes the immune checkpoint inhibitors (ICI) nivolumab and pembrolizumab, and in 2020, the FDA approved the first combination therapies (atezolizumab/bevacizumab and nivolumab/ipilimumab) in HCC (Finn *et al.*, 2020). However, despite significant therapeutic advance with ICI, ~75% of patients do not respond to these immunotherapies for unclear reasons (Giraud et al., 2021). More recently, a meta-analysis of three randomized phase III clinical trials administering ICI to patients with advanced HCC showed a superior efficacy of immunotherapies in virally-infected patients compared to NASH-affected patients with HCC (Pfister et al., 2021). This suggests that the tumor microenvironment (TME) of HCC is an important determinant of therapeutic success and highlight the urgent need to further explore human liver-specific immunity towards the identification of theranostic immune biomarkers for patients stratification and novel immunotherapies.

Myeloid cells are a main immune infiltrate in several solid tumors and considered as an impediment to all cancer therapeutic modalities, particularly immunotherapy. Thus, modulating their recruitment, differentiation or functions is being actively pursued as a therapeutic option (Goswami et al., 2022). However, their indiscriminate depletion has failed to improve cancer patient overall survival, indicating that a better characterization of the deleterious myeloid subsets is required for a targeted approach. Myeloid cells encompass mononuclear phagocytes (MNP) (including monocytes, macrophages and dendritic cells [DC]) and granulocytes, which exhibit remarkable heterogeneity and divergent functions according to ontogeny, tissue microenvironment, proximal inflammatory and metabolic signals and trained immunity elicited epigenetic reprogramming. The advent of single cell and tracing technologies have unraveled the complexity of myeloid states, warranting context-specific characterization of deleterious immunosuppressive and pro-tumoral subsets to direct targeted therapies.

102 While the cellular landscape of HCC has been previously described using single cell
103 RNA sequencing (scRNA-seq) and mass cytometry (Ma et al., 2019; Ma et al., 2021; Sharma
104 et al., 2020; Song et al., 2020; Sun et al., 2021; Zhang et al., 2019; Zheng et al., 2017), the
105 impact of etiology on the diversity of the innate immune compartment, particularly myeloid
106 cell states, has not been fully characterized. Here, we implemented scRNA-seq on purified
107 hepatic innate immune cells freshly isolated from tumoral and juxta-tumoral tissues from
108 patients with HCC of different etiologies, and performed spatial transcriptomics (stRNA-seq)
109 to map their localization. We unravel a steatohepatitis-associated contexture characterized by
110 enhanced myeloid biased NK cell differentiation and the emergence of entropic myeloid cell
111 states. Among the myeloid populations, we identify three *THBS1*+ myeloid cell subsets with
112 features previously linked to a suppressive state (Condamine et al., 2016). Among these, one
113 discrete population was abundant in the tumor of patients with steatohepatitic HCC but absent
114 in patients with viral HCC in our cohort. We show that this population expresses a variety of
115 myeloid lineage-affiliated genes, including granulocyte, macrophage and dendritic cell
116 features, and can be identified in HCC tumors based on selective dual expression of TREM1
117 and CD163. Through functional characterization, we demonstrate that $TREM1^{+}CD163^{+}$
118 myeloid cells are potent suppressors of T cell effector functions *ex vivo*, a function further
119 potentiated by TREM1 engagement. Our results reveal that $TREM1^{+}CD163^{+}$ M_{reg} express high
120 levels of TGFβ and IL-13RA and are spatially enriched at HCC fibrotic lesions in close
121 association with FAP^{+} cancer-associated fibroblasts. Deconvolution analyses in large cohorts
122 of patients with HCC reveals that the intra-tumoral density of $TREM1^{+}CD163^{+}$ M_{reg} population
123 increases in advanced stages and associates with poor prognosis according to different
124 molecular classifications. In a separate cohort of patients with renal cell carcinoma, the density
125 of $TREM1^{+}CD163^{+}$ M_{reg}, but not that of any other MNP subset characterized in our study, also
126 associates with therapeutic resistance to PD-1 blockade. Our results elucidate this population
127 as a biomarker of severe HCC and a therapeutic target in patients resistant to immunotherapy.

128 **RESULTS**

129

130 **The hepatic innate immune landscape in HCC**

131 To characterize the innate immune cellular landscape of the liver from patients with HCC, we
132 implemented scRNA-seq (10x Genomics) on FACS-sorted CD45^{+} panTCRαβ^{-} CD19^{-} innate
133 immune cells freshly isolated from tumors (HCC) and adjacent non-tumoral (NT) liver sections.
134 In parallel, we applied spatial transcriptomics (ST; Visium®, 10x Genomics) on frozen tissue
135 sections from the same patients (Figure 1a). We included 10 HCC patients with different
136 etiologies (HCV (n=3), obesity (n=5), excessive alcohol consumption (n=3)) (Figure S1a and
137 Table S1). NASH (n=3) and cirrhotic lesions (n=3) were confirmed in HCC and NT tissue
138 sections by hematoxylin eosin saffron and trichrome staining (Figure S1b). For the scRNA-seq,
139 for each of the 20 fresh samples, 15,000 innate immune viable cells were loaded on the 10x
140 chip. Following putative doublet removal and exclusion of stressed or dead cells (Figure S1c),
141 we analyzed the transcriptomes of ~96,000 single innate immune cells (~2,300 genes/cell)
142 across 10 HCC (~46,000 cells) and 10 NT (~50,000 cells) samples. Following data processing
143 using the SEURAT pipeline, 22 Louvain clusters were identified (Figure 1b), containing cells
144 derived from all patients and tissue sites (Figure 1c and Table S2). Using a scoring method
145 based on published signatures retrieved from Panglao DB (Table S3), combined with the
146 expression of discriminatory features (Figure 1d and Table S4) and canonical markers (Figure
147 1e), we identified the major hepatic innate immune cell populations (Figure 1f). In total, we
148 identified 11 innate lymphoid clusters (~68,000 cells), encompassing one innate lymphoid cell
149 (ILC) cluster (c20) and 10 clusters of NK cells. These included one cycling NK cluster (c16),
150 two NK1 clusters (c0, 2) representing *CD56*^{low} *CD16*$^{+}$ cytotoxic NK cells, four NK2 clusters
151 (c1, 4, 6, 9) representing inflammatory *CD56*^{high} *CD16*$^{-}$ NK cells, two mixed NK3/γδ T cell
152 clusters (c3, 15), and one small NK4 cluster (c13). In addition, we identified 10 myeloid clusters
153 (~28,000 cells) including four monocyte/macrophage (Mo/Mac) clusters (c5, 7, 10, 14), two
154 conventional DC clusters (c11, 17), one plasmacytoid DC (pDC) cluster (c19) and three
155 granulocyte clusters (neutrophils (c12), mast cells (c18) and basophils (c21)). Besides the
156 expected myeloid cells, our analysis revealed a population of cells found primarily on the
157 myeloid side of the Louvain graphical representation (c8, green) (Figure 1f), expressing both
158 lymphoid (*IL7R, GNLY, KLRF1, KLRD1*, *GZMH/K/B, IFNG*) and myeloid genes (*LYZ*, *HLA-*
159 *DRA/B1, S100A8/9, SAT1, CST3*) (Figure 1d [box] and Figure S2). We refer to this population
160 as myeloid NK (MyeNK), as characterized below. Next, to assess the tumoral distribution of

161 the identified innate immune cell subsets, we quantified cluster frequencies in HCC compared
162 to NT. This analysis revealed significant intra-tumoral depletion of NK2 cells and enrichment
163 of Mo/Mac subsets (Figure 1g, h), and such TME remodeling is exacerbated with cancer
164 progression (Figure 1i). Altogether, our results define the landscape of innate immune cells in
165 HCC, confirm significant myeloid cell infiltration in tumors and unravel a distinct population
166 of cells with the unique property of dually expressing innate lymphoid and myeloid genes.
167
168 **Phenotypic and functional characterization of myeloid NK cells**
169 NK cells expressing myeloid genes have been previously described in mice as precursors to
170 mature NK (pre-mNK) (reviewed in (Guimont-Desrochers and Lesage, 2013)). In addition,
171 both mature NK (Theurich et al., 2017) and γδ T (Howard et al., 2017) cells can acquire myeloid
172 properties in pathological conditions, notably in obesity (Theurich *et al.*, 2017). To unravel the
173 identity of cells in c8, we first selected genes that clearly distinguish lymphoid from myeloid
174 cell subsets in our data, namely *NKG7, KLRD1, LYZ* and *HLA-DRA* (Figure S2a). We next
175 ascertained dual expression of these NK/lymphoid and myeloid features on a per cell basis.
176 This analysis showed that the majority of cells co-expressing these genes belonged to c8 (Figure
177 S2b). Cell trajectory analysis using Slingshot revealed that c8 occupied a central position along
178 the Pseudotime between lymphoid and myeloid lineages (Figure S2c). To distinguish among
179 the innate lymphoid subpopulations, we next tested two signatures capable of distinguishing
180 NK cells from ILCs (Heinrich et al., 2021) or γδ T cells (*CD3D*, *CD3E*, *TRDC* and *TRGC2*)
181 (Pizzolato et al., 2019) (Table S5). Cells in c8 scored highest for the NK gene signature (Figure
182 S2d). Taken their segregation with the myeloid transcriptomes (Figure 1f), we posited that c8
183 is a population of myeloid-biased NK cells. Phenotypically, they were $CD56^{low}$ (*NCAM1*)
184 $CD16^{+}$ (*FCGR3A*), expressed cytotoxic factors (*GZMB, GZMK, IFNG*), NK activating
185 receptors (*CD160*) but low levels of markers associated with tissue homing (*EOMES, ITGAE*)
186 (Figure S2e). This phenotype suggests that MyeNK cells are mature cytotoxic effectors. To
187 confirm this, we conducted computational tests and functional validation. Computationally, we
188 estimated differentiation potency by calculating entropy rates (or signaling promiscuity), which
189 is useful to distinguish precursor states (high entropy rates) from fully differentiated cells (low
190 entropy rates). This analysis revealed that, unlike cycling NK (cNK) cells that displayed high
191 entropy rates, MyeNK cells had the lowest entropy rates compared to all other innate immune
192 cells analyzed, indicative of a differentiated state (Figure S2f). For functional validation, we
193 first confirmed the detection of these cells in HCC surgical resections by multiplex

194 immunofluorescence (IF) e.g. cells co-expressing GNLY and HLA-DR, and flow cytometry
195 (FACS) e.g. cells co-expressing KLRD1 and HLA-DR (Figure S2g, h). Notably, compared to
196 MNPs, HLA-DR was expressed at intermediate levels on MyeNK cells both at the transcript
197 (Figure S2b, bottom) and protein (Figure S2h) levels. We next FACS-isolated them based on
198 the co-expression of KLRD1 and HLA-DR (gated on $CD45^+$ $CD19^-$ panTCRαβ$^-$, panTCRγδ$^-$
199 cells) and assessed their lytic capacity in an *ex vivo* killing assay. These experiments showed
200 that similar to NK cells, MyeNK cells responded to IL-2+IL-15 and were highly cytotoxic
201 (Figure S2i, j). In addition, as for other NK cells, MyeNK cells were found at lower proportions
202 in HCC compared to NT, representing 3,3% and 5,9% of all hepatic innate immune cells,
203 respectively (Figure 1g). Re-clustering of the MNP transcriptomes unraveled two clusters of
204 MyeNK cells (c2, 5) (Figure 2a and S2k, l). c2 originated mostly from one patient, whereas c5
205 contained cells from all patients (Table S2). MyeNK cells (c5) were poorly represented in the
206 tumor (Figure S2k), but increased in the juxta-tumoral tissue of obese- and/or NASH-affected
207 patients with HCC (Figure S2l). Altogether, our results identify a myeloid-biased NK cell
208 population that is expanded in the liver of obese/NASH-affected patients.
209
210 **Specific populations of MNP infiltrate HCC primary tumors**
211 To investigate MNP diversity and distribution in HCC, we re-clustered their transcriptomes. A
212 total of 19 Louvain clusters were identified, including 17 clusters of MNPs and two clusters of
213 MyeNK (c2, 5) (Figure 2a). The MNP clusters encompassed macrophages (c10, 17), a spectrum
214 of monocyte-like states (c0, 1, 3, 4, 7, 9, 15, 16), monocyte-derived DC (moDC; c6) and DCs
215 (c8, 11, 12, 13, 14, 18). *FCN1* expression marked moDCs and all monocyte states (Figure 2b).
216 Among these, three clusters (c0, 3, 4), discriminated by the selective expression of *THBS1*,
217 referred to as *THBS1*_Myeloid (*THBS1*_M), were enriched for signatures ascribed to myeloid-
218 derived suppressor cells (MDSCs) (Condamine *et al.*, 2016) (Figure 2b, c and Table S4). The
219 other clusters (c1, 7, 9, 15, 16) expressed highest levels of *LILRB1, LILRB2* and *POU2F2*
220 (Figure 2b, Table S4), features associated with differentiated monocytes (Weinreb et al., 2020).
221 These could be classified according to *CD14* and *FCGR3A* (CD16) expression, into
222 *CD14*$^+$*CD16*$^-$ classical monocytes (cMono) (c1, 16), *CD14*$^+$*CD16*$^+$ intermediate monocytes
223 (iMono) (c7) and *CD14*$^-$*CD16*$^+$ non-classical monocytes (ncMono) (c9, 15). A core signature
224 (Table S5) of 6 genes (*SELENOP, APOE, C1QA, CD81, FOLR2, TREM2*) distinguished
225 macrophages (c10, 17) from other innate immune cells (Figure S3a-d; Figure 2b, c). c10
226 expressed highest levels of *FOLR2*, previously described as a marker of tissue-resident

macrophages (TRM) (Nalio Ramos et al., 2022), whereas c17 was discriminated by the expression of *SPP1* (Figure 2b), which marks tumor-associated macrophages (TAMs). However, c17 also expressed *FOLR2* at lower level, and Kupffer cell (KC) features e.g., *MARCO* and *TIMD4* (Figure 2c), suggesting mixed populations. To refine the macrophage characterization, we re-clustered c10 and c17, which distinguished seven macrophage subsets (Figure 2d): one inflammatory (c6; *IL1B, CD83, CD86*), two *FOLR2*$^{-}$*TREM2*$^{+}$ (c1, 3), expressing in common *CD9, SPP1* and *GPNMB* among others, and four *FOLR2*$^{+}$*TREM2*$^{-}$ (c0, c2, c4, c5) (Figure 2d, e). The latter included KC (c4; *MARCO, TIMD4*) and three TRM-like clusters expressing higher levels of *MRC1 (CD206)* (Figure 2e and S4a). A previous study implicated NOTCH signaling in re-programming a subset of bone marrow (BM)-derived macrophages into *FOLR2*$^{+}$ TRM-like macrophages (Sharma *et al.*, 2020). Cells in c2 expressed high levels of the NOTCH effector *HES1* (Figure 2e) and scored highly for our TRM signature (Figure S4b), suggesting that they might represent such a population. As reported in (Sharma *et al.*, 2020), they highly expressed *LYVE1* (Figure 2e), which marks peri-vascular localization. Furthermore, our analysis revealed that among the *TREM2*$^{+}$*SPP1*$^{+}$ cells, two subsets can be distinguished based on differential expression of *CD163,* a *CD163*^{low} subset (TAM1 (c1)) with discriminatory expression of metallothioneins (*MT1X, MT1G, MT2A*), and a *CD163*^{high} subset (TAM3 (c3)) expressing several immune checkpoints at higher levels compared to other TAM populations, including *HAVCR2* (TIM3), *LGALS9* (Galectin-9), *VSIR* (VISTA), *CD58* and the metabolic immune checkpoint interleukin-4-induced-1 (*IL4L1*) (Sadik et al., 2020) (Figure 2f). Notably, all three TAM subsets were enriched in HCC compared to NT in our patient cohort, while KCs were depleted (Figure 2g).

To explore the heterogeneity of DCs in HCC, we re-clustered the DC transcriptomes, which identified one DC1 cluster (c2) expressing *CLEC9A, XCR1* and *DNASE1L3*, one AS-DC (c8) expressing *AXL* and *SIGLEC6*, one migratory DC (migDC, c7) (Miller et al., 2012), also referred to as mature regulatory DCs (Maier et al., 2020), expressing maturation and migration genes *(LAMP3, CCL19, CCR7)*, and four DC2 states expressing in common *CD1C* and *CLEC10A*. *FCER1A* marked DC2 (c0, 1), with (c1) distinguished by high expression of *CD163*. c4 found in HCV-infected HCC patients exhibited a type I IFN signature *(IFITM3, GBP5, GBP1, VAMP5),* while c5 shared features with moDC, expressing monocyte-associated genes *(FCN1, S100A8/9),* and was marked by high *THBS1* expression. In addition, two clusters of pDC (c3, 6) were identified expressing *JCHAIN, LILRA4, MZB1,* and *IL3RA* (Figure 2h, i). Among the DC subsets, migDCs were significantly enriched in the tumor tissue of all patients

260 in our cohort (Figure 2j), and DC2 (c4) found in HCV-infected patients were also enriched in
261 HCC compared to NT (Figure 2j).

262 To confirm in large cohorts of patients the MNP subsets infiltrating HCC primary
263 tumors, we next used the deconvolution algorithm CIBERSORTx (Steen et al., 2020), trained
264 with our scRNA-seq data to predict cell-type density in bulk transcriptomics datasets. We first
265 interrogated two cohorts of patients with HCC, i.e., TCGA_LIHC (371 patients) and GSE76427
266 (115 patients) (Grinchuk et al., 2018). We also explored MNP subset densities in two unrelated
267 cohorts of patients with lung adenocarcinoma (TCGA_LUAD; 515 patients) and colon
268 adenocarcinoma (TCGA_COAD; 285 patients). Our results show a consistent tumoral
269 depletion of *FOLR2*_TRM (c10) in all cohorts (Figure 2k), in line with findings in human breast
270 cancer (Nalio Ramos *et al.*, 2022). In contrast, iMono (c7) and moDC (c6) are more abundant
271 in the tumor compared to NT in all cohorts. With the exception of LIHC, migDC (c11) infiltrate
272 the tumor in most cohorts, i.e., LUAD, COAD and GSE76427, consistent with our scRNA-seq
273 results (Figure 2k). cMono (c1) and ncMono (c9) are inversely correlated in HCC, with lower
274 cMono (c1) proportions in the tumors. However, this tissue distribution is not consistent in
275 LUAD and COAD (Figure S4c), suggesting HCC-specific regulation. Surprisingly, the three
276 MDSC-like *THBS1*_M subsets, do not display similar patterns of tumoral infiltration. Whereas
277 *THBS1*_M (c0) are depleted from the tumor in HCC and LUAD, *THBS1*_M (c4) significantly
278 infiltrate the tumor along with moDC (c6) and iMono (c7) in all cohorts (Figure 2k). The
279 densities of *THBS1*_M (c3) and *SPP1*_Mac (c17) is variable among tissues and across cohorts
280 (Figure S4c). Similar results were obtained when we deconvoluted using subset expression
281 profiles from the macrophage and DC re-clustering. This analysis further unraveled a pDC
282 subset (c3) that infiltrate tumors in HCC and LUAD, and two inflammatory DC2 subsets (c4,
283 c5) as additional tumor-infiltrating MNPs in all cohorts (Figure 2k).

284 Since HCC etiology might underlie the heterogeneity of response to ICB in patients
285 with HCC (Pfister *et al.*, 2021), we took advantage of our scRNA-seq data to assess the impact
286 of etiology on myeloid cell diversity in HCC tumors. Our results show that among the tumor-
287 infiltrating MNPs, *THBS1*_M (c4) cluster was exclusively found in patients with steatohepatitis
288 but not in viral HCC (Figure S4d, e). ncMono (c9, 15) and DC2 (c12) also expanded in this
289 condition (Figure S4d, e). In contrast, iMono (c7) and moDC (c6) were less abundant in
290 steatohepatitis compared to viral HCC (Figure S4d, e). Collectively, our results identify iMono,
291 moDC, inflammatory DC2 and the MDSC-like *THBS1*_M (c4) subset, as universal tumor-

292 infiltrating MNPs (TIMs) and unravel an effect of steatohepatitis on intra-tumoral MNP states,
293 particularly an expansion of the MDSC-like *THBS1*_M (c4) population.
294
295 **Fine-mapping MDSC-like states in HCC**
296 Despite their significance in cancer progression, MDSCs are poorly annotated, and the
297 phenotypic markers used to isolate them overlap with those of normal neutrophils and
298 monocytes in both mice and humans (Veglia et al., 2021). Our analysis revealed three clusters
299 of *THBS1*_M cells enriched in MDSC signatures (Condamine *et al.*, 2016). These outnumbered
300 TAMs in HCC, representing 27.4% of all MNP analyzed (c0, 10.8%; c3, 8.4%; c4, 8.2%)
301 (Figure 2a). To better characterize them, we first elucidated a core signature of 10 genes
302 (*THBS1, TREM1, S100A12, SERPINB2, OLR1, SAP30, PHLDA1, MEGF9, VEGFA, VCAN*)
303 that identified them primarily in c10 (and c5 to a lower extent) in the innate immune dataset
304 (Figure 3a, b), and distinguished them from other MNP (Figure S3m, n). They were selectively
305 marked by *THBS1,* and expressed both monocyte-lineage (*FCN1*) and neutrophil-lineage
306 (*CSF3R*) genes, but were not fully differentiated monocytes (*POU2F2*) (Weinreb *et al.*, 2020).
307 *TREM1* encoding 'Triggering receptor expressed on myeloid cells 1', highly expressed in
308 neutrophils (Figure 3c), discriminated the three *THBS1*_M clusters from other MNPs (Figure
309 3d). The lectin type oxidized LDL (oxLDL) receptor 1 (LOX-1, encoded by *OLR1*), previously
310 described as a specific marker of human PMN-MDSC (Condamine *et al.*, 2016), marked c0
311 (Figure S5a-c). However, it was also detected in other monocytes at lower levels (Figure S5b,
312 c), as reported in (Travaglini et al., 2020). In contrast, we identified *SERPINB2* that encodes
313 the plasminogen activator inhibitor type 2 as a more robust marker of *THBS1*_M (c0) (Figure
314 S5a-c). *MEGF9* (Multiple EGF Like Domains 9) was most highly expressed in *THBS1*_M (c3),
315 while SAP30 (Sin3A Associated Protein 30) discriminated *THBS1*_M (c4) (Figure S5a, b). In
316 order to elucidate the nature of the three *THBS1*_M subsets, we next performed an analysis of
317 differentially expressed genes (DEG). This revealed that genes highly expressed in neutrophils
318 e.g. *CXCL8, NAMPT* and *PLAUR* were also highly expressed in c0 as compared to c3/c4
319 (Figure 3e and Table S6), suggesting that c0 might encompass cells with a PMN-MDSC-like
320 state. c3 was discriminated from c4 by monocyte lineage genes *ATF3, CD14, CSF3R, CACYBP,*
321 *LGALS2, LILRA5* (Figure 3f and Table S6), suggesting that it may represent an M-MDSC-like
322 state. In contrast, c4 had multi-lineage gene expression; its top DEGs encompassed
323 macrophage- and DC-lineage genes (*C1QA/B/C, CD163* and *CLEC10A, CST3*), in addition to
324 genes shared with c0 (*NAMPT, OLR1, PHLDA1/2, PLAUR*) (Figure 3f, g and Table S6). To

325 explore the dynamic regulation of the three *THBS1*_M subsets, we next mapped their position
326 along an inferred trajectory through Pseudotime ordering, which revealed three main states
327 (Figure 3h). Analysis of temporally expressed genes along the Pseudotime identified the
328 different profiles including a state expressing a variety of myeloid lineage genes at intermediate
329 levels (Figure 3i). This subset was marked by high expression of inflammatory cytokine
330 receptor genes e.g. *IL1RN, IL6R* and the inflammasome gene *NLRP3* (Figure 3i). Calculation
331 of differentiation potency estimates revealed that the 'multi-lineage' *THBS1*_M (c4) had higher
332 entropy rates compared to *THBS1*_M (c0), *THBS1*_M (c3) and *SPP1*_Mac (c17) (Figure 3j).
333 Monocle2 pseudotime trajectory analysis revealed that *THBS1*_M (c4), moDC (c6) and iMono
334 (c7) occupied an intermediate state along the pseudotime (Figure S5d). Similar results were
335 obtained on Principal Component analysis of all MNP subsets, which segregated monocytes,
336 from macrophages and DCs, and revealed intermediate states for *THBS1*_M (c4), moDC (c6),
337 iMono (c7) as well as migDC (c11) (Figure S5e). Predicted ordering by CYTOTRACE further
338 supported the intermediate state of these subsets between DCs and macrophages/classical
339 monocytes (Figure S5f). Unlike *THBS1*_M (c4), *THBS1*_M (c0) and *THBS1*_M (c3) exhibited
340 a more committed state and segregated closer to differentiated monocytes (Figure S5e, f).
341 Together, our results unravel a discrete population of MDSC-like cells (*THBS1*_M (c4)) that
342 consistently infiltrate tumors and are distinguished from other MNPs by 'multi-lineage'
343 expression of granulocyte and macrophage/DC genes.
344

345 **TREM1$^+$ CD163$^+$ myeloid cells are super immunosuppressors**

346 We next sought to investigate the function of the three *THBS1*_M populations. We searched for
347 surface proteins differentially expressed among them. We found that the scavenger receptor
348 CD36 was highly expressed on all three *THBS1*_M subsets compared to macrophages (Figure
349 3k) and other MNPs (Figure 2c). Among the *THBS1*_M subsets, *OLR1* was mainly expressed
350 in *THBS1*_M (c0) with intermediate levels in *THBS1*_M (c4), whereas CD163 was highly
351 expressed in *THBS1*_M (c4) (Figure 3k). Flow cytometry analysis of CD163 and LOX-1
352 revealed mutually exclusive staining within the CD45$^+$CD3$^-$CD19$^-$CD56$^-$CD36$^+$ population
353 (Figure 3l). Consistent with our scRNA-seq data, surface expression of TREM1 was more
354 prominent on the LOX-1$^+$CD163$^-$ (*THBS1*_M (c0)) and LOX-1$^-$CD163$^+$ (*THBS1*_M (c4))
355 populations, as compared to LOX-1$^-$CD163$^-$ (*THBS1*_M (c3)) cells (Figure 3m). The
356 *THBS1*_M (c4) subset can thus be identified as the main immune population in HCC dually
357 expressing TREM1 and CD163. Because of their high entropy and enrichment in MDSC

358 signature genes, we next functionally assessed their immunosuppressive activity. We FACS-
359 sorted the three subsets from surgical resections of patients with HCC and co-cultured them
360 with a high avidity Th1-polarized $CD4^+$ T cell clone reactive to the tumor-associated antigen
361 (TAA) Telomerase (TERT) peptide UCP4, as in (Lauret Marie Joseph et al., 2020). All three
362 subsets inhibited the production of IFNγ by $CD4^+$ T cells upon UCP4 stimulation, but the
363 $TREM1^+CD163^+$ population showed the most potent inhibitory effect (Figure 3n and S5g). As
364 a control, we generated human monocyte-derived suppressor cells (HuMoSc) *ex vivo* according
365 to an established protocol (Janikashvili et al., 2015), and confirmed that they were highly
366 efficient in suppressing cytokine production by activated T cells (Figure S5h, i). Interestingly,
367 phenotypic characterization of these HuMoSc showed that they were primarily $CD163^+$ (>85%)
368 and highly expressed TREM1 on their surface (Figure S5j, k), suggesting that a strong
369 immunosuppressive capacity can be identified by dual expression of TREM1 and CD163 on
370 monocytic cells. Myeloid cells exert their immunosuppressive functions through different
371 mechanisms. e.g. via reactive oxygen species (ROS), nitric oxide (NO), arginase, prostaglandin
372 E2 (PGE_2), anti-inflammatory cytokines (e.g. IL-10, TGFβ) and cell surface immune
373 checkpoints such as PD-L1 (Hegde et al., 2021). Interrogation of the expression of central
374 effectors in these pathways revealed that *$TREM1^+CD163^+$* myeloid cells (*THBS1*_M (c4))
375 expressed highest levels of *TGFB1* (Figure 3o), which was also observed in *ex vivo* generated
376 HuMoSc (Figure S5l). They also exhibited highest levels of *IL13RA*, which encodes a chain of
377 the receptor for IL-13, a cytokine implicated in TGFβ induction (Fichtner-Feigl et al., 2006;
378 Lee et al., 2001). In addition, they had elevated levels of *PTGES2* and *PTGER2,* encoding a
379 PGE2 synthase and receptor, respectively, as well as *ODC1,* encoding ornithine decarboxylase
380 that acts downstream of arginase as the rate-limiting enzyme in the polyamine biosynthesis
381 pathway. In addition, they shared with *THBS1*_M (c0) high expression of *ATF4* (encoding
382 Activating Transcription Factor 4, an endoplasmic reticulum (ER) stress effector recently
383 demonstrated to be required for MDSC immunosuppressive function (Halaby et al., 2019))
384 (Figure 3o). Collectively, these results uncover a discrete population of regulatory myeloid cells
385 (M_{reg}), identified in HCC as $TREM1^+CD163^+$, with potent immunosuppressive function.
386

387 ***$TREM1^+CD163^+$* M_{reg} cells are enriched at fibrotic lesions in HCC**

388 Liver fibrosis is a dominant precursor of HCC irrespective of etiology and the IL-13-TGFβ1
389 axis is a major driver of this process (Chiaramonte et al., 1999; Nakamura et al., 2000; Roulot
390 et al., 1999). TGFβ activates hepatic stellate cell (HSC), promotes their function in extracellular

391 matrix remodeling and collagen deposition (Hellerbrand et al., 1999), and mediates resistance
392 to anti-PD-L1 treatment (Mariathasan et al., 2018). IL-13 receptor signaling elicits TGFβ
393 production (Fichtner-Feigl *et al.*, 2006; Lee *et al.*, 2001), but also cooperates with it in
394 independently inducing the expression of pro-fibrotic genes such as matrix metalloproteases
395 (MMPs), tissue inhibitors of metalloprotease-1 (TIMP1) and interstitial collagens (Gieseck et
396 al., 2016; Kaviratne et al., 2004), and IL13RA blockade has been shown to inhibit hepatic
397 fibrosis (Chiaramonte *et al.*, 1999). Our results revealed highest expression of *IL13RA* and
398 *TGFB1* in *TREM1*$^{+}$*CD163*$^{+}$ myeloid cells (*THBS1*_M (c4)). We therefore wondered whether
399 these cells were associated with HCC fibrotic lesions. To this end, we performed spatial
400 transcriptomics (ST) on tumor tissue sections from patients with HCC. Two patients had
401 confirmed fibrosis: patient #20 had severe fibrosis (Metavir, F3) linked to alcohol consumption,
402 while patient #23 had moderate fibrosis (Metavir, F1/F2) linked to NASH (Table S1). Fibrotic
403 lesions were evident on the H&E-stained tissue sections processed for ST (Figure 4a, f).
404 Transcriptomics from 2261 and 1987 spots were obtained at a median depth of 34,526 and
405 26,017 UMIs/spot, and 5882 and 4954 genes/spot for patients # 20 and #23, respectively (Table
406 S7). Unbiased clustering identified eight clusters in patient #20 and ten clusters in patient #23
407 (Figure 4b, g). Based on spot feature expression of a fibrosis-associated signature (*COL1A1*,
408 *TIMP1, ACTA2*), we identified clusters 2 and 5 in patient #20, and cluster 8 in patient #23 as
409 scoring highly for the fibrosis signature (Figure 4c-d, h-i). We next interrogated the *in situ*
410 expression of a geneset composed of four genes (*TREM1, VCAN, THBS1, S100A4*) collectively
411 discriminating *THBS1*_M cells from other innate immune cells (Figure 4k). Our results revealed
412 a striking overlap in the expression of this gene signature with that marking fibrotic lesions
413 (Figure 4d-e, i-j). *VCAN, THBS1* and *S100A4* may also be expressed by fibroblasts indicating
414 that *THBS1*_M cells are geared with a pro-fibrotic machinery, consistent with their high
415 expression of *TGFB1* (Figure 3o) and *TIMP1* (Figure 4k). To ensure specific detection of
416 *TREM1*$^{+}$*CD163*$^{+}$ M_{reg} cells, we next examined the expression of a more-restricted signature
417 composed of *TREM1, CD163* and *CLEC4E* that discriminates this subset from other MNPs
418 (Figure 2c and Table S4). Our results revealed that *TREM1*$^{+}$*CD163*$^{+}$ M_{reg} cells populate fibrotic
419 lesions (Figure 4d-e, i-j).
420 The heterogeneity of fibroblasts shapes the tumor immune microenvironment and is
421 associated with the outcome of cancer progression (Davidson et al., 2021; Peltier et al., 2022).
422 Specific cancer-associated fibroblast (CAF) sub-populations promote immunosuppression in
423 the TME and have been linked to immunotherapy resistance (Kieffer et al., 2020; Qi et al.,

424 2022). Immunosuppressive CAFs exhibit an activated phenotype and express markers such as
425 fibroblast-activation protein (*FAP*) and components of the desmoplastic structures, including
426 collagens (*COL1A1, COL3A1*), integrins (*ICAM1*) and tissue factor (*F3*). We interrogated the
427 spot feature expression of a FAP$^+$ CAF signature (*FAP, COL1A1*, *ICAM1, F3*) in our ST data
428 and observed overlapping spatial distribution with that of *TREM1*$^+$*CD163*$^+$ M$_{reg}$ (Figure 4d-e,
429 i-j), suggesting potential crosstalk between these two populations. To validate this observation
430 in a larger cohort of HCC patients, we used CIBERSORTx deconvolution to predict the
431 abundance of MNP subsets defined in our study and that of 7 CAF populations defined by
432 scRNA-seq in (Qi *et al.*, 2022), namely *FAP*_fibroblasts, MFAP5_myofibroblasts, proliferating
433 fibroblasts, *CD24*_fibroblasts, *FGFR2*_fibroblasts, *CD73*_fibroblasts and DES_fibroblasts.
434 Our results show that *FAP*_fibroblasts, *MFAP5*_myofibroblasts and proliferating fibroblasts
435 were enriched in the tumors of HCC patients, whereas *CD24*_fibroblasts were not (Figure 4l).
436 We next performed Pearson correlations to assess infiltration patterns of MNP and CAF
437 subsets. We observed significant positive correlations between *TREM1*$^+$*CD163*$^+$ M$_{reg}$ and
438 *FAP*_fibroblasts, *MFAP5*_myofibroblasts and proliferating fibroblasts (Figure 4m, n). The
439 same correlations were observed for iMono (c7), ncMono (c9), moDC (c6) and DC2 (c8).
440 Together, these results point to a specific spatial co-localization of *TREM1*$^+$*CD163*$^+$ M$_{reg}$ with
441 pro-fibrogenic, immunosuppressive CAFs in tumors from patients with HCC.
442

443 **_TREM1_$^+$_CD163_$^+$ M$_{reg}$ correlate with poor clinical outcomes and reduced survival in**
444 **patients with HCC and predict resistance to immune checkpoint blockade**

445 Suppressive myeloid cells are collectively considered as tumor promoting and an impediment
446 to efficient anti-tumor immunity. Our data revealed significant tumor infiltration of
447 *TREM1*$^+$*CD163*$^+$ M$_{reg}$ in several cohorts of patients with solid tumors, including HCC (Figure
448 2k). TREM1$^+$CD163$^+$ M$_{reg}$ have superior immunosuppressive activity (Figure 3m) and
449 specifically associate with tumor-promoting and immunosuppressive *FAP*$^+$ CAFs (Figure 4m).
450 Therefore, we wondered whether *TREM1*$^+$*CD163*$^+$ M$_{reg}$ are associated with worse survival in
451 patients with HCC. We first explored the median expression of the *THBS1*_M core signature
452 geneset (Table S5) in the TCGA_LIHC cohort. Patients with higher expression of this geneset
453 have significantly poorer mean overall survival (mOS) (Figure 5a). We next used
454 CIBERSORTx deconvolution to interrogate MNP associations with tumor grade. PMN-
455 MDSC-like *THBS1*_M (c0), M-MDSC-like *THBS1*_M (c3), *FOLR2*_Mac (c10), and
456 *SPP1*_Mac (c17) are not associated with this parameter (Figure S6a). In contrast,

457 *TREM1*$^{+}$*CD163*$^{+}$ M_{reg} significantly associate with higher pathological tumor grade (stages III
458 and IV) (Figure 5b), consistent with our scRNA-seq data in which cells of this subset were
459 exclusively derived from patients with high grade HCC (patients #20 and #23; Table S2).
460 iMono (c7) and moDC (c6) are also enriched in higher grade tumors (Figure 5b). Second, we
461 assessed links with serum alpha-fetoprotein (AFP) levels, an important prognostic factor and a
462 predictive biomarker of mortality (Tsukuma et al., 1993). Among the *THBS1*_M populations,
463 only the proportion of *TREM1*$^{+}$*CD163*$^{+}$ M_{reg} strongly correlates with elevated AFP (Figure 5c),
464 whereas M-MDSC-like *THBS1*_M (c3) are counter-correlated (Figure S6b). iMono and moDC
465 have significant albeit weaker associations with this clinical parameter (Figure 5c). Third, we
466 examined associations with the inactivation of HIPPO, as defined by the silence of HIPPO
467 [SOH] signature, reported to predict poor prognosis in patients with HCC (Sohn et al., 2016).
468 The proportions of *TREM1*$^{+}$*CD163*$^{+}$ M_{reg} and moDC but not that of other MNPs are higher in
469 the SOH class of patients compared to patients with active HIPPO signaling (AH) (Figure 5d
470 and S6c). Last, we interrogated an integrative classification by Hoshida *et al.* that stratifies
471 patients according to molecular and clinical features (Hoshida et al., 2009). As for pathologic
472 tumor grade, serum AFP and SOH, the proportion of *TREM1*$^{+}$*CD163*$^{+}$ M_{reg} are highest in the
473 Hoshida S2 subclass, characterized by larger and poorly differentiated tumors, elevated serum
474 AFP and poor mOS (Figure S6d). M-MDSC-like *THBS1*_M (c3) do not associate with the
475 Hoshida classification, whereas the proportions of PMN-MDSC-like *THBS1*_M (c0) and
476 *FOLR2*_Mac decrease with HCC severity (S3→S1→S2) (Figure S6d). Collectively, these
477 results identify *TREM1*$^{+}$*CD163*$^{+}$ M_{reg}, moDC and iMono as the main tumor-infiltrating MNPs
478 that associate with poor prognosis in patients with HCC, according to the measured clinical
479 parameters.

480 Next, we wondered whether the nature of the myeloid infiltrate could stratify HCC
481 patients and serve as an immunological biomarker of clinical outcomes. To address this, we
482 performed hierarchical unsupervised clustering of HCC patients in the TCGA_LIHC cohort
483 based on CIBERSORTx predicted proportions of the MNP populations we characterized in this
484 study. Tumor-infiltrating MNP profiles divided HCC patients into three strata (Figure S6e) with
485 significantly different mOS (Figure 5e). Group A patients with the best mOS have higher
486 proportions of *FOLR2*_Mac and *THBS1*_M (c0) (Figure S6e, f), i.e., the two MNP subsets
487 generally depleted from solid tumors (Figure 2k), whereas higher *SPP1*_Mac proportions
488 distinguishes group B patients with an intermediate mOS (Figure S6e, f). Group C patients,
489 with markedly reduced mOS, are characterized by the highest proportions of *TREM1*$^{+}$*CD163*$^{+}$

490 M_{reg} (*THBS1*_M (c4)), moDC and iMono (Figure 5f and S6e, f). Notably, the proportions of
491 *TREM1*$^+$*CD163*$^+$ M_{reg} in this cohort correlate with regulatory T cells (T_{reg}), exhausted CD8$^+$ T
492 cells and neutrophils, according to expression profiles defined by scRNA-seq in (Qi *et al.*, 2022)
493 (Figure 5g). Last, we wished to examine myeloid subsets association with resistance to immune
494 checkpoint blockade (ICB). Because we did not have access to transcriptomic data from study
495 cohorts of patients with HCC treated with ICB, we interrogated datasets from other solid
496 tumors. In a cohort of 181 patients with advanced clear cell renal cell carcinoma (ccRCC)
497 treated with anti-PD-1 in prospective clinical trials (Braun et al., 2020), *TREM1*$^+$*CD163*$^+$ M_{reg}
498 density significantly associates with progressive disease (PD) (Figure 5h). None of the 18 other
499 MNP cell subsets defined in this study correlate with immunotherapy resistance in this cohort
500 (Figure S6g). Together, our results identify *TREM1*$^+$*CD163*$^+$ M_{reg} as a potent
501 immunosuppressive tumor-infiltrating myeloid population associated with poor prognosis in
502 HCC and resistance to ICB described in ccRCC.
503
504 **TREM1 associates with poor prognosis in solid tumors and confers immunosuppression**
505 Among the 10 genes constituting the *THBS1*_M core signature, *TREM1* confers the highest
506 hazard ratio on HCC survival in the TCGA_LIHC cohort (Figure 3a). Patients with high
507 *TREM1* expression have significantly poorer mOS than patients with lower expression (Figure
508 6a), consistent with previous reports in other HCC patient cohorts (Duan et al., 2015; Liao et
509 al., 2012). Our findings that *TREM1*$^+$*CD163*$^+$ M_{reg} are highly immunosuppressive and predict
510 poor prognosis in HCC prompted us to interrogate whether *TREM1* expression *per se* is
511 associated with poor clinical outcomes, and if it plays a direct role in immunosuppression. We
512 first interrogated *TREM1* expression in the three HCC patient groups from the TCGA_LIHC
513 cohort classified according to MNP infiltration profiles. We observed highest expression of
514 *TREM1* in group C patients (Figure 6b), enriched in *TREM1*$^+$*CD163*$^+$ M_{reg} and with a poor
515 mOS (Figure 5e, f). In addition, *TREM1* expression is higher in patients with fibrosis, and
516 significantly associates with the silence of HIPPO (SOH) and the Hoshida S2 class (Figure 6b).
517 *TREM1* positively correlates with several effectors of immunosuppression, most significantly
518 with *TGFB*, *IL10, PTGES2* and *IL8* (Figure 6f), as well as with *PTGER2* and *CD274* (PD-L1)
519 (Figure S7a). Besides HCC, *TREM1* expression also associates with high pathologic tumor
520 grades in other solid tumors, namely colon and rectum adenocarcinoma and kidney renal clear
521 cell carcinoma, as revealed in TCGA_COAD, TCGA_READ and TCGA_KIRC cohort
522 analyses, respectively (Figure S7b). Furthermore, *TREM1* expression significantly associates

523 with resistance to anti-PD-1 revealed in the GSE78220 cohort of patients with melanoma (Hugo
524 et al., 2017) (Figure S7c). Together, these results point to TREM1 as a potential effector of
525 tumor progression and immunosuppression. To experimentally address the role of TREM1 in
526 cancer immunity, we investigated its expression and function in mouse models of liver injury
527 (Farrell et al., 2019), NASH and HCC *in vivo*, as well as in human monocyte cultures *ex vivo.*
528 We used obese *db/db* diabetic mice fed a methionine and choline-deficient diet (MCD) for 7
529 weeks to elicit NASH, and carbon tetrachloride (CCL4)-treatment of C57Bl/6J mice as a model
530 of liver injury (Figure S7d, e). In both disease models, mice had elevated levels of circulating
531 liver enzymes, namely aspartate aminotransferase (AST) and alanine aminotransferase (ALT),
532 indicative of liver damage (Figure S7f). In the NASH model, mice had elevated triglycerides,
533 as expected, compared to control or CCL4-treated mice (Figure S7f). Immunophenotyping of
534 the liver revealed enhanced accumulation of TNFα-producing $CD8^+$ T cells in both NASH-
535 affected or CCL4-treated mice (Figure S7g). In contrast, a significant influx of $TREM1^+$
536 $CD11b^+$ $Ly6C^+$ $Ly6G^-$ myeloid cells was observed in the NASH setting but not in control mice
537 and to a lesser extent in CCL4-treated mice (Figure S7h), accompanied by an induction of
538 TREM1 surface expression (Figure S7i), consistent with our scRNA-seq results revealing the
539 *TREM1*$^+$*CD163*$^+$ M_{reg} subsets in steatohepatitis-affected patients with HCC (Figure S4d, e). To
540 address the role of TREM1 in HCC, we next used the Hep55.1C liver orthotopic mouse model
541 of HCC and inhibited TREM1 signaling using the GF9 peptide (Shen and Sigalov, 2017) that
542 interferes with TREM1 binding to its signaling adaptor DAP12. Our results show that pan-
543 blockade of TREM1 signaling promoted tumor eradication (Figure S7j), as observed by others
544 in different animal models (Wu et al., 2012; Wu et al., 2019). However, since the GF9 peptide
545 could modulate TREM1 functions in immune and non-immune compartments, we next used
546 the *ex vivo* HuMoSc model in co-culture with T cells to formally examine the role of TREM1
547 in the immunosuppressive functions of myeloid cells. Treatment of HuMoSc cells with the
548 TREM1 ligand PGLYRP1 (peptidoglycan recognition protein 1) in complex with
549 peptidoglycan (PGN) (PP) significantly increased cell surface expression of TREM1 (Figure
550 6g), and induced LOX-1 and CD15 (Figure 6h). In addition, it resulted in heightened production
551 of IL-10 and IL-8 (Figure 6i), and processing and release of soluble TREM1 (sTREM1) (Figure
552 6i). Importantly, TREM1 stimulation led to potent suppression of T cell proliferation (Figure
553 6j) and effector functions, e.g. inhibition of TNFα production (Figure 6k). Together, these
554 results suggest that the steatohepatitis-environment promotes the genesis of $TREM1^+$ M_{reg} cells

555 with strong immunosuppressive and pro-tumoral functions, and point to *TREM1* as a potential
556 immunotherapeutic target in HCC.
557
558 **Discussion**
559 Here, investigation of the innate immunity hepatic cellular landscape of patients with HCC
560 revealed previously unreported transcriptional and phenotypic states of different innate
561 lymphoid and myeloid cells. Our work reports four novel findings with important clinical
562 implications: 1) HCC-associated genesis of cells exhibiting mixed lymphoid and myeloid
563 identities as well as cells with inter-myeloid mixed states, potentially stemming from
564 emergency myelopoiesis and trained immunity responses to tumor growth (Mulder et al., 2019;
565 Pietras et al., 2016; Sica et al., 2019); 2) a heterogeneity of myeloid states, yet with only specific
566 subsets infiltrating the tumor; 3) identification of a TREM1^{+}CD163^{+} M_{reg} subset with strong
567 immunosuppressive activity that expands in the steatohepatitis setting, populates fibrotic
568 lesions in HCC, and associates with poor prognosis in HCC; and 4) demonstration of a role of
569 TREM1 in amplifying the immunosuppressive function of human monocyte-derived
570 suppressor cells and promoting HCC growth *in vivo*.
571 The first observation applies particularly to a population of cytotoxic cells scoring
572 highly for an NK signature yet segregating with myeloid cells in a UMAP visualization. Cells
573 with similar properties have been previously described primarily in mouse models of cancer,
574 and while they were initially thought to be DCs acquiring a 'killer' capacity (Chan et al., 2006;
575 Taieb et al., 2006), they were later shown to derive from lymphoid progenitors in the bone
576 marrow (Blasius et al., 2007; Caminschi et al., 2007; Vosshenrich et al., 2007) and renamed
577 pre-mature NK (pre-mNK) (Guimont-Desrochers et al., 2012). Our results argue that myeNK
578 are not pre-mNK for several reasons: a) trajectory analysis positioned MyeNK nearest to NK4
579 cells, which is a fully differentiated NK state; b) potency differentiation analysis similarly
580 highlighted that both MyeNK and NK4 are the least entropic compared to other NK cells,
581 particularly cycling NKs that in contrast has high entropy rates suggestive of a precursor state;
582 and c) MyeNK were highly cytotoxic as demonstrated functionally in a cancer-killing assay,
583 which is at odds with a pre-mature state. Our single cell analysis unravels the expansion of
584 myeNK in the NASH setting, particularly in the juxta-tumoral tissue. Metabolic signals or
585 inflammatory mediators induced by metabolic dysregulation might thus drive their genesis,
586 recruitment to the liver and/or acquisition of myeloid features. This is in line with Theurich *et*
587 *al.* who reported obesity-associated IL-6-dependent induction of an NK population with

588 myeloid properties (Theurich *et al.*, 2017). Cells expressing both cytotoxic and myeloid genes
589 have also been reported in human blood (Villani et al., 2017) and HCC (Sun *et al.*, 2021).
590 However, in these studies, they were referred to as monocytes, without further characterization.
591 We posit that MyeNK cells stem from an inflammatory signal amplified in the steatohepatitis
592 setting. Whether the strong cytotoxic capacity of MyeNK is beneficial in NASH-HCC remains
593 to be clarified.

594 Another phenomenon elicited in the tumor setting presumably through emergency
595 myelopoiesis is the genesis and recruitment of MDSCs (Loftus et al., 2018). Our analysis
596 demonstrates a significant heterogeneity in myeloid populations enriched in MDSC signature
597 genes (Condamine *et al.*, 2016), warranting reclassification of MDSCs according to more
598 precise phenotypic and functional properties (Hegde *et al.*, 2021). We show that *THBS1*
599 expression marks myeloid cells enriched in MDSC genes (Condamine *et al.*, 2016). They were
600 found in three distinct states in HCC, including one with dual granulocyte- and
601 macrophage/DC-lineage features, identified as *TREM1*$^{+}$*CD163*$^{+}$. Our results show that this
602 subset exhibits a more potent immunosuppressive activity compared to other *THBS1*_M cells,
603 strongly inhibiting T cell proliferation and effector functions *ex vivo*. We show, using spatial
604 transcriptomics, that this subset highly populates fibrotic lesions in HCC in close associations
605 with pro-fibrogenic and pro-tumorigenic fibroblast subsets. This subset was exclusively found
606 in patients with steatohepatitis HCC in our cohort. Consistently, using *in vivo* models of liver
607 disease, we observed a NASH-associated expansion of TREM1^{+} myeloid cells among the
608 CD11b^{+}LY6C^{+}LYC6G^{+} population, which is consistent with the reported reliance of MDSC
609 on cellular lipid metabolism (Veglia *et al.*, 2021) and upregulated cell surface expression of
610 lipid receptors and transporters, notably the oxidized low-density lipoprotein (oxLDL)
611 receptors CD36 and LOX-1 (*OLR1*) and the fatty acid transporter FATP2 (Veglia et al., 2019).
612 This was accompanied by notable TREM1 induction on this subset in NASH, that was not
613 observed in control mice and to a much lower extent in liver injury induced by CCL4 treatment.
614 In line with a recent report demonstrating progressive accumulation of CD8^{+}TNF^{+}PD-1^{+} T cells
615 in the NASH-affected liver that exacerbates HCC in a mouse model in a CD8^{+} T cell- and TNF-
616 dependent manner (Pfister *et al.*, 2021), we observed enhanced hepatic infiltration of
617 CD8^{+}TNF^{+} T cells in NASH, but this was not unique to this condition, as it was also observed
618 in CCL4-treated mice. Thus, besides CD8^{+}TNF^{+} T cell infiltration, NASH also elicits TREM1^{+}
619 M_{reg} recruitment, which might underlie resistance to immunotherapy.

620 TREM1, a cell surface receptor expressed on monocyte-derived inflammatory
621 macrophages and neutrophils, has been previously described as an amplifier of inflammation
622 (Bouchon et al., 2001). It was initially proposed to promote HCC development through pro-
623 inflammatory cytokine production by Kupffer cells (Wu et al., 2012). However, this early
624 analysis used a non-discriminatory staining that marks a heterogeous group of myeloid cells,
625 preventing precise identification of deleterious myeloid cell subsets. Our scRNA-seq data
626 reveal that TREM1 is a discriminatory feature of *THBS1*_M cells distinguishing them from
627 other MNPs including monocytes, macrophages/TAMs and DCs in the liver of HCC patients.
628 Among these, we identify a *TREM1*$^{+}$*CD163*$^{+}$M$_{reg}$ subset as a potent immunosuppressive
629 population that associates with poor prognosis in HCC. We show that *TREM1* expression *per*
630 *se* is predictive of poor clinical outcomes in several solid tumors and with ICB resistance.
631 TREM1 has been implicated in mediating liver fibrosis (Nguyen-Lefebvre et al., 2018) and
632 immunotherapy resistance in a mouse model of liver cancer (Wu *et al.*, 2019). However, the
633 underlying mechanisms have not been fully explored. Functionally, we demonstrate that
634 TREM1 ligation by cognate ligand on human monocyte-derived suppressor cells promotes their
635 acquisition of features linked to a suppressive phenotype, such as enhanced expression of LOX-
636 1, CD15 and IL-10, and boosts their capacity to suppress T cell proliferation and effector
637 functions.
638 Collectively, our study supports the stratification of patients according to HCC etiology
639 to define optimal therapeutic regimens, and points to TREM1 targeting as an attractive
640 therapeutic option in NASH-associated HCC.
641
642
643
644
645 **Authors' contributions.** All authors revised the manuscript and approved the final version.
646
647 **Conflict of interest statement**
648 The authors declare that the research was conducted in the absence of any commercial or
649 financial relationships that could be construed as a potential conflict of interest.
650
651 **Acknowledgements**
652 We thank the TBMCore flow cytometry platform operator Vincent Pitard, Marlène Maître at
653 the Magendie Neuro center, Sébastien Marais at the Bordeaux Imaging Center, Aurélia Le
654 Dantec, Gaël Galli and Sébastian Lillo for help and advice. We also thank the Bordeaux
655 Bioinformatic Center (CBiB) for computational resources. This work is funded by operating
656 grants to MS from the ARC foundation, IDEX Bordeaux and ITMO cancer and an
657 infrastructure grant to MS from the New Aquitaine region. JG and DC are funded by the ARC

foundation grant and ER received a studentship from the SIRIC BRIO. JG, DC and ER also received salary funding from the New Aquitaine region.

660

661 **Figure Legends**

662 **Figure 1. The innate immunity landscape of the liver of patients with hepatocellular**
663 **carcinoma (HCC)**
664 (A) Multi-omics characterization of the hepatic innate immune cell landscape of human
665 patients with hepatocellular carcinoma (HCC) using scRNA-seq and stRNA-seq of tumors
666 and adjacent NT of 10 HCC patients with different etiologies.
667 (B) Louvain clustering of 96,229 scRNA-seq transcriptomes of hepatic innate immune cells in
668 two tissue sites from 10 HCC patients identifies 22 main clusters in the liver.
669 (C) UMAP visualization colored according to patient ID and their respective cell number
670 recovery according to tissue.
671 (D) Heatmap representing average expression of discriminating genes for each cluster.
672 (E) Feature Plots representing the expression of innate immune cells canonical markers.
673 (F) Louvain clusters shown in (B) colored based on cell type annotation.
674 (G) Main cluster frequencies in HCC and NT. *p<0.05 multiple Wilcoxon tests.
675 (H) UMAP colored by tissue site, HCC (blue) and NT (grey).
676 (I) Circular plot representing cluster frequencies in NT and HCC of different tumor grades.
677

678 **Figure 2. Defining MNP subsets and their predicted tumoral distribution.**
679 (A) Louvain clustering of 25,146 MNP transcriptome libraries colored based on cell type
680 annotation.
681 (B) Violin plots depicting the expression per cluster of selected discriminating genes
682 (C) Dot plot depicting average expression (dot color) per cluster of selected discriminating
683 genes and percentage of cells (dot size) expressing those genes.
684 (D) Louvain re-clustering of macrophages (MNP clusters 10 and 17) identifies 7 new clusters
685 of KC, TRMs, TAMs and an inflammatory *IL-1B*_Mac subset.
686 (E) Dot plot depicting average expression per cluster of selected discriminating genes
687 (F) Dot plot depicting average expression of immune checkpoint genes in TAMs.
688 (G) Macrophage cluster frequencies in the adjacent NT (grey) versus HCC (blue) of the 10
689 patients investigated by scRNA-seq. *p<0.05 using multiple Wilcoxon tests
690 (H) Louvain re-clustering of DCs (MNP clusters 8, 11, 12, 13, 14 and 18)
691 (I) Dot plot depicting average expression per cluster of selected discriminating genes
692 (J) DC cluster frequencies in the adjacent NT and HCC of the 10 patients investigated by
693 scRNA-seq. *p<0.05 using multiple Wilcoxon tests
694 (K) Box plots depicting the predicted proportions of MNP subsets by CIBERSORTx
695 deconvolution of bulk transcriptomics datasets from four cohorts of patients, with either HCC
696 (TCGA_LIHC; GSE76427), colon adenocarcinoma (TCGS_COAD) or lung adenocarcinoma
697 (TCGA_LUAD). Signatures derived from the MNP re-clustering were used, except for the
698 boxplots of DC2 (c4, c5) generated using DC re-clustering signatures.
699

700 **Figure 3. Identification of *TREM1*$^{+}$*CD163*$^{+}$ M$_{reg}$ cells as potent immunosuppressive**
701 **myeloid cells.**
702 (A) *THBS1*_M (c10) core signature specificity and association with mOS in patients with HCC
703 from TCGA_LIHC cohort. HR, hazard ratio
704 (B) Violin plots depicting the signature score of *THBS1*_M 10 genes-core signature in the
705 different innate immune main clusters.
706 (C) Violin plots depicting the expression per cluster of selected discriminating genes in the
707 different innate immune main clusters.

708 (D) Density plot representing the expression of *TREM1* as a discriminatory marker of the three
709 *THBS1*_M clusters.
710 (E) Volcano plot depicting differentially expressed genes between *THBS1*_M (c0) and other
711 *THBS1*_M cells (c3+c4).
712 (F) Volcano plot depicting differentially expressed genes between *THBS1*_M (c3) and
713 *THBS1*_M (c4).
714 (G) Heatmap representing expression of selected genes from CIBERSORTx top 60 genes in
715 (c4) for 100 cells in each cluster shown.
716 (H) Pseudotime trajectory analysis using Monocle2 of the three THBS1_M clusters, colored by
717 monocle state, Pseudotime or cluster.
718 (I) Heatmap of the top temporally expressed genes identifying the different Monocle2 states.
719 (J) Box plots of signaling entropy values (y-axis, also named potency) in the three *THBS1*_M
720 clusters and the *SPP1*_Mac cluster.
721 (K) Violin plots depicting expression of *CD36, OLR1* and *CD163* in the indicated MNP
722 clusters.
723 (L) Gating strategy used to sort human *THBS1*_M (c0, c3 and c4 of the MNP dataset) subsets
724 according to differential expression of LOX-1 and CD163 in the $Lin^{-}CD36^{+}$ population.
725 M) Histograms depicting TREM1 expression among the different *THBS1*_M subsets according
726 to differential expression of LOX-1 and CD163 in the $Lin^{-}CD36^{+}$ population.
727 (N) Quantification of the % inhibition of IFNγ production by a TERT-specific $CD4^{+}$ T cell
728 clone stimulated or not with UCP4 TERT peptide in co-culture with different *THBS1*_M subsets
729 sorted from HCC surgical resections according to the gating strategy in (L).
730 (O) Dot plot depicting average expression per cluster of genes associated with myeloid
731 immunosuppressive functions.
732
733 **Figure 4. *TREM1*$^{+}$*CD163*$^{+}$ M_{reg} cells populate fibrotic lesions in HCC**
734 (A-J) Tumor tissue sections from two patients with HCC (P20, P23) were analyzed by stRNA-
735 seq using the Visium platform from 10x Genomics.
736 (A, F) Tumor tissue sections stained with H&E
737 (B, G) Overlapping spatial localization of spatial Louvain Seurat clusters
738 (C, H) Spatial scoring of a gene signature marking fibrosis (*ACTA2, TIMP1, COL1A1*)
739 (D, I) Spatial scoring of gene signatures identifying FAP^{+} cancer-associated fibroblasts
740 (CAFs) (*FAP, COL1A1, ICAM1, F3*) (left), *THBS1*_M (*TREM1, VCAN, THBS1, S100A4*)
741 (middle) and *TREM1*$^{+}$*CD163*$^{+}$ M_{reg} (*TREM1, CD163, CLEC4E*) (right).
742 (E, J) Violin plots depicting signature score of the interrogated spatial genesets in each Seurat
743 cluster.
744 (K) Dot plots depicting average expression per cluster of genes associated with fibrosis or
745 expressed in *THBS1*_M in the innate immunity dataset (left) or MNP dataset (right).
746 (L) Box plots depicting the predicted proportions of fibroblast subsets by CIBERSORTx
747 deconvolution of bulk transcriptomics data from the TCGA_LIHC cohort.
748 (M) Matrix of Pearson correlations from predicted proportions of MNP and fibroblast subsets
749 deconvoluted from the TCGA_LIHC cohort data. Green, positive correlation; Pink, negative
750 correlation
751 (N) Scatter plots depicting Pearson correlations between proportions of *TREM1*$^{+}$*CD163*$^{+}$ M_{reg}
752 and different fibroblast subsets.
753
754 **Figure 5. *TREM1*$^{+}$*CD163*$^{+}$ M_{reg} correlate with poor prognosis in HCC and resistance to**
755 **immune checkpoint blockade.**

(A) Kaplan-Meier survival curves of patients with HCC (n=364) (Menyhart et al., 2018) according to expression of the *THBS1*_M core signature.
(B-D) Box plots depicting the predicted proportions of MNP subsets by CIBERSORTx deconvolution of bulk transcriptomics data from the TCGA_LIHC cohort according to tumor grade (Low, pathologic T grade 1 and 2; High, pathologic T grade 3 and 4) (B), serum AFP (<300 or >300) (C), or HIPPO status (D).
(E) Kaplan-Meier survival curves of patients with HCC (n=193) from TCGA_LIHC cohort stratified according to MNP infiltrate profiles.
(F) Box plots depicting the predicted proportions of MNP subsets according to patient group from (E).
(G) Scatter plots depicting Pearson correlations between proportions of *TREM1*$^+$*CD163*$^+$ M_{reg} and exhausted CD8$^+$ T cells or neutrophils, and Pearson correlations between proportions of neutrophils and exhausted CD8$^+$ T cells.
(H) Box plots depicting the predicted proportions of *TREM1*$^+$*CD163*$^+$ M_{reg} according to patient response to anti-PD-1 (Nivolumab) in a cohort of patients with clear cell renal cell carcinoma (ccRCC).

Figure 6. TREM1 associates with poor prognosis in solid tumors and promotes the immunosuppressive function of M_{reg} cells.
(A) Kaplan-Meier survival curves of patients with HCC (n=364) (Menyhart *et al.*, 2018) according to *TREM1* expression.
(B) Box plots depicting the average expression of *TREM1* according to MNP infiltrate profiles, fibrosis, HIPPO status or Hoshida class.
(C) Scatter plots depicting Pearson correlations between the expression of *TREM1* and genes associated with immunosuppression (*TGFB, IL10, IL8* and *PTGES2*).
(D) Histograms depicting TREM1 expression on HuMoSc treated on day 6 of differentiation with PBS or a PP complex of peptidoglycan (PGN) and PGN recognition protein 1 (PGLYRP1) for 24 hours.
(E) Representative FACS scatterplot depicting cells positive for the expression of CD14 (y-axis), LOX-1 (x-axis, top) and CD15 (x-axis, bottom) as in (D).
(F) Bar graphs depicting the concentration of IL-10, IL-8 and soluble TREM1 (sTREM1) released from HuMoSc treated with PBS or PP as in (D).
(G) Representative FACS histogram depicting CellTrace Violet dilution as a readout of CD3$^+$ T cell proliferation for 6 days in the listed conditions
(H) Quantification of the % inhibition of TNFα production by a CD3$^+$ T cells stimulated or not with anti-CD3/CD28 in co-culture with HuMoSc pre-treated withf PBS or PP as in (D).

SUPPLEMENTAL FIGURES AND TABLES

Figure S1. Related to Figure 1
(A) Clinical characteristics of the patients included in this study. Complete information is provided in Table S1.
(B) HES staining of NT and tumoral tissue sections from all patients in the study.
(C) Pipeline of scRNA-seq bioinformatic analyses

Figure S2. Identification of a MyeNK population in HCC depleted from the tumor and associated with good prognosis

802 (A) Violin plots depicting the expression levels of lymphoid (*NKG7, KLRD1*) and myeloid
803 (*LYZ, HLA-DRA*) features in the different innate immunity main clusters.
804 (B) Scatter graphs depicting clusters containing single versus double positive cells for the
805 expression of *NKG7* and *LYZ* or *KLRD1* and *HLA-DRA*.
806 (C) Slingshot trajectory analysis identifying MyeNK at the intersection between myeloid and
807 lymphoid lineages.
808 (D) Violin plots depicting the scores of NK versus γδ T cell signatures in the different innate
809 immunity main clusters.
810 (E) Violin plots depicting the expression levels of NK features in the different innate immunity
811 main clusters.
812 (F) Scatterplot of signaling entropy (SE) against Slingshot Pseudotime values. Low SE is
813 indicative of a differentiated state.
814 (G) Multiplex immunofluorescence staining of HLA-DR (green) and GNLY (red) expression;
815 DAPI marks nuclei (blue).
816 (H) Representative FACS scatterplot depicting cells positive for the expression of HLA-DR
817 (red), KLRD1 (blue) and HLA-DR^{+} KLRD1^{+} double positive cells (green). FMO, fluorescence
818 minus one.
819 (I) Scatterplots depicting Pacific Blue-positive dead K562 cells killed by NK2 (CD56^{med}), NK1
820 (KLRD1^{+} HLA-DR^{-}) or MyeNK (KLRD1^{+} HLA-DR^{+}) cells isolated by FACS sorting from
821 liver of human patients with HCC (n=3), in *in vitro* co-culture experiments.
822 (J) Quantification of dead cells from the *in vitro* killing assay, as in (H). One of two
823 representative experiments is shown. Data represent the mean +/- SEM.
824 (K) Left, MyeNK (c5) frequencies in the adjacent NT versus HCC of the 10 patients
825 investigated; right, UMAP colored by tissue site, HCC (blue) and NT (grey). **$p<0.01$ using
826 Mann-Whitney tests.
827 (L) Left, UMAP of cells in NT colored by obesity status, obese (dark blue), non-obese (light
828 blue); right, MyeNK (c5) frequencies in NT according to NASH status. *$p<0.05$ using Mann-
829 Whitney tests.
830
831 **Figure S3. Related to Figure 2**
832 (A) Core Mac signature specificity and association with mOS in patients with HCC. HR, hazard
833 ratio.
834 (B) Violin plots depicting the score of Mac core signature in the different innate immunity main
835 clusters.
836 (C) Violin plots depicting the score of Mac core signature in the different MNP clusters.
837 (D) Core Mac signature specificity applied to the two Mac clusters of the MNP dataset (c10,
838 17) and association with mOS in patients with HCC. HR, hazard ratio
839 (E) Core cDC signature specificity and association with mOS in patients with HCC. HR, hazard
840 ratio.
841 (F) Violin plots depicting the score of cDC core signature in the different innate immunity main
842 clusters.
843 (G) Violin plots depicting the score of cDC core signature in the different MNP clusters.
844 (H) Core cDC signature specificity applied to the four cDC clusters of the MNP dataset (c8, 11,
845 12, 13) and association with mOS in patients with HCC. HR, hazard ratio
846 (I) Core pDC signature specificity and association with mOS in patients with HCC. HR, hazard
847 ratio.
848 (J) Violin plots depicting the score of pDC core signature in the different innate immunity main
849 clusters.
850 (K) Violin plots depicting the score of pDC core signature in the different MNP clusters.

851 (L) Core pDC signature specificity applied to the two pDC clusters of the MNP dataset (c14,
852 16) and association with mOS in patients with HCC. HR, hazard ratio
853 (M) Violin plots depicting the score of *THBS1*_M core signature in the different MNP clusters.
854 (N) Core *THBS1*_M signature specificity applied to the three *THBS1*_M clusters of the MNP
855 dataset (c0, 3, 4) and association with mOS in patients with HCC. HR, hazard ratio
856 (O) Core neutrophils signature specificity and association with mOS in patients with HCC. HR,
857 hazard ratio.
858 (P) Violin plots depicting the score of neutrophils core signature in the different innate
859 immunity main clusters.
860 (Q) Core mast cells signature specificity and association with mOS in patients with HCC. HR,
861 hazard ratio.
862 (R) Violin plots depicting the score of mast cells core signature in the different innate immunity
863 main clusters.
864 (S) Core basophils signature specificity and association with mOS in patients with HCC. HR,
865 hazard ratio.
866 (T) Violin plots depicting the score of basophils core signature in the different innate immunity
867 main clusters.
868
869 **Figure S4. Related to Figure 2**
870 (A) A schematic illustration summarizing marker gene expression in the different macrophage
871 subsets in HCC; TAMs (pink), TRMs (green).
872 (B) Violin plots depicting the score of TAM versus TRM signatures
873 (C) Box plots depicting the predicted proportions of MNP subsets by CIBERSORTx
874 deconvolution of bulk transcriptomics datasets from four cohorts of patients, with either HCC
875 (TCGA_LIHC; GSE76427), colon adenocarcinoma (TCGS_COAD) or lung adenocarcinoma
876 (TCGA_LUAD).
877 (D) UMAP of cells in HCC+NT colored by viral (green) or steatohepatitis (brown) positive
878 status.
879 (E) Donut plot depicting MNP cell proportions in HCC according to steatohepatitis positive
880 status (brown).
881
882 **Figure S5. Related to Figure 3**
883 (A) Dot plot depicting average expression per cluster of top discriminating genes.
884 (B) Density plots representing the expression of discriminating genes marking the three
885 *THBS1*_M clusters universally (top) or selectively (bottom).
886 (C) Violin plots depicting the expression levels of discriminating genes in the different innate
887 immunity main clusters.
888 (D) Pseudotime trajectory analysis using Monocle2 of the three *THBS1*_M clusters together
889 with those encompassing macrophages (c10, 17), moDC (c6) and monocytes (c1, 7, 9, 15, 16)
890 from the MNP dataset.
891 (E) Principal Component Analysis of 300 cells from all MNP clusters.
892 (F) Predicted ordering of differentiation by CytoTRACE analysis
893 (G) Representative FACS scatter plots depicting intracellular IFNγ staining in TERT-specific
894 $CD4^+$ T cells stimulated or not with PMA/ionomycin or a TERT peptide (UCP4) in the presence
895 or absence of myeloid cells with differential expression of TREM1 and LOX-1
896 (H) Representative FACS scatter plots depicting intracellular IFNγ staining in $CD3^+$ T cells
897 stimulated or not with anti-CD3/CD28 in the presence or absence of HuMoSc at the indicated
898 co-culture ratios.

(I) Quantification of the % inhibition of IFNγ and TNFα production by $CD3^+$ T cells stimulated or not with anti-CD3/CD28 in the presence or absence of HuMoSc at the indicated co-culture ratios.
(J) Phenotypic characterization of HuMoSc using the gating strategy in (Figure 3L), and histograms depicting TREM1 expression among the different subsets.
(K) Quantification of the frequencies of $TREM1^+$ cells among the different HuMoSc gates shown in (J).
(L) Expression of *COL1A1, TIMP1* and *TGFB1* in HuMoSc and fibroblasts cultures, measured by quantitative RT-PCR. Note that *COL1A1* is not expressed in HuMoSc.

Figure S6, related to Figure 5
(A-D) Box plots depicting the predicted proportions of MNP subsets by CIBERSORTx deconvolution of bulk transcriptomics data from the TCGA_LIHC cohort according to tumor grade (A), serum AFP (B), HIPPO status (C) or Hoshida class (D).
(E) Heatmap depicting estimated proportions of MNP subsets derived from CIBERSORTx in HCC patients from the TCGA_LIHC cohort
(F) Box plots depicting the predicted proportions of MNP subsets according to patient group from (E).
(G) Box plots depicting the predicted proportions of MNP subsets according to patient response to anti-PD-1 (Nivolumab) in a cohort of patients with clear cell renal cell carcinoma (ccRCC).

Figure S7, related to Figure 6
(A) Scatter plots depicting Pearson correlations between the expression of *TREM1* and *PTGER2* (left) or *CD274* (right).
(B) Box plots depicting *TREM1* expression according to tumor grade in three cohorts of solid tumors, TCGA_COAD (colon adenocarcinoma), TCGA_READ (rectum adenocarcinoma) and TCGA_KIRC (kidney renal cell carcinoma).
(C) Box plots depicting *TREM1* expression according to patient response to anti-PD-1 in a cohort of patients with metastatic melanoma.
(D) Study design for the mouse models of NASH and fibrosis and mouse body weight from a representative experiment.
(E) H&E staining of liver tissue sections from mice of the indicated condition. Scale bar, 250μm.
(F) AST, ALT and triglycerides (TG) serum concentration in C57BL/6J mice treated with CCL4 (green) and db/db mice fed a MCD-diet (red). Age-matched C57BL6J mice were used as controls (blue).
(G) Percentage of $CD8^+TNF^+$ cells among $CD3^+$ T cells.
(H) Percentage (%) of $CD11b^+LY6C^+LY6G^-$ (left panel) and $TREM1^+CD11b^+LY6C^+LY6G^-$ (middle panel).
(I) Mean fluorescence intensity (MFI) quantification (left panel) and a representative histogram (right panel) of TREM1 in $TREM1^+CD11b^+LY6C^+LY6G^-$ in the indicated mouse groups.
(J) Tumor volume by luminescence quantification in a liver orthotopic transplantable model of HCC using Hep55.1C cell-line transduced with a lentivirus encoding luciferase. Mice were treated with a vehicle control peptide or the GF9 peptide (i.p.) three times a week at 25 mg/kg starting on day 7 post tumor cells inoculation.

947

948 **TABLE S1. Patient Characteristics**

Advanced HCC patients	**#12**	**#13**	**#14**	**#16**	**#17**	**#18**	**#19**	**#20**	**#23**	**#24**
Sex, male/female (m/f)	f	m	m	m	m	m	m	m	m	m
Age, years	68	63	62	85	78	78	60	74	70	69
Bilirubin, mg/dL	11	10	16	11	9	8	44	7	10	18
Albumin level (g/L)	38.3	32	33.3	36.9	32.4	24.6	39.9	40.7	39.2	40.9
INR	1.2	0.98	1.24	1.05	0.97	1.37	1.17	0.96	0.96	0.92
Neutrophil/Lymphocyte ratio	2.60	2.42	3.04	2.97	1.76	1.17	1.34	1.82	3.10	1.56
MELD score	8	6	9	7	7	10	12	8	7	7
Child Pugh Score	A	A	A	A	A	B	A	A	A	A
Liver fibrosis, METAVIR score ; F0-F2/F3/F4	A0F3	A1F2	A0F1	F1A0	F0F1	F3	F0/F1	F3	F1/F2	F0/F1
Body Mass Index	32	39	24	22,8	19,7	25,3	32,4	26,6	30,2	31,4
Etiology of liver disease										
Alcohol	no	yes	no	no	no	no	yes	yes	no	no
Steatohepatitis	no	yes	no	no	no	yes	yes	yes	yes	no
NASH	no	yes	no	no	no	yes	no	no	yes	no
HCV/HBV	HCV	no	no	HCV	no	no	no	no	no	HCV
Alpha fetoprotein, ng/mL	6580	4.6	6.4	6.1	n.d.	3	96.6	78.8	3.1	4.7
Number of HCC nodules/liver ; 1/2/3/>4	1	>4	1	>4	1	1	1	1	1	1
Mean largest size of HCC, mm	54 x 50 x40	72 x 72 x 60	85 x 60 x 50	38 x 33 x 30	24 x 18 x 16	27 x 25 x 22	40	95 x 60 x 50	55 x 45 x 40	19 x 17 x 10
Macrovascular invasion	no	yes	no	no	no	no	no	no	no	no
Extrahepatic metastasis	no	no	no	no	no	no	no	no	no	no
Grade (Edmondson-Stainer)	III	II-III	III	II	II	II	II-III	III-IV	III-IV	II-III
Treatment, chemoembolization	yes	no	yes	no	no	yes	no	no	no	no

949

950 Non-alcoholic steatohepatitis (NASH); international normalized ratio (INR); neutrophil-to-
951 lymphocyte ratio (NL ratio); Model for end-stage liver disease (MELD); Barcelona Clinic Liver
952 Cancer system (BCLC).
953

954 **SUPPLEMENTAL TABLES (SEPARATE EXCEL FILES)**
955
956 **TABLE S2. CELL NUMBER PER CLUSTER AND SUBCLUSTER**
957
958 **TABLE S3. PANGLAO LISTS**
959
960 **TABLE S4. DISCRIMINATING GENES LIST_TOP 100**
961
962 **TABLE S5. SIGNATURES**
963
964 **TABLE S6. *THBS1*_M DEGs**
965
966 **TABLE S7. VISIUM WEB SUMMARY**
967
968 **TABLE S8. DATA PROCESSING SUMMARY**
969

970 **STAR METHODS**

971 **1) KEY RESOURCES**

REAGENT or RESOURCE	**SOURCE**	**IDENTIFIER**
Antibodies		
anti-Human CD11c (clone 3.9) BV711	BioLegend	Cat#301630
anti-Human CD16 (clone 3G2) AF700	BioLegend	Cat#302026
anti-Human CD163 (clone REA812) PE-Vio 770	Miltenyi	Cat#130-112-130
anti-Human CD19 (clone REA675) APC Vio770	Miltenyi	Cat#130-113-643
anti-Human CD19 (cloneREA675) VioBright R720	Miltenyi	Cat#130-127-382
anti-Human CD19 (clone REA675) PE Vio770	Miltenyi	Cat#130-113-647
anti-Human CD3 (clone REA613) APC Vio 770	Miltenyi	Cat#130-113-136
anti-Human CD36 (clone REA760) FITC	Miltenyi	Cat#130-110-739
anti-Human CD4 (clone M-T466) PE Vio 770	Miltenyi	Cat#130-113-255
anti-Human CD45 (clone H130) FITC	BioLegend	Cat#304054
anti-Human CD45 (clone REA747) Viogreen	Miltenyi	Cat#130-110-638
anti-Human CD56 (clone REA196) Viobright TM 515	Miltenyi	Cat#130-114-552
anti-Human CD56 (clone REA196) APC-vio770	Miltenyi	Cat#130-114-548
anti-Human CD56 (clone REA196) PE Vio 770	Miltenyi	Cat#130-113-313
anti-Human CD69 (clone FN50) PE-Cy5	BD Biosciences	Cat#555532
anti-Human CD94 (clone REA113) APC	Miltenyi	Cat#130-098-976
anti-Human HLA-DR (clone REA805) FITC	Miltenyi	Cat#130-111-788
anti-Human IFN-γ (clone REA600) APC	Miltenyi	Cat#130-113-495
anti-Human LOX-1 (clone REA1188) APC	Miltenyi	Cat#130-122-111

anti-Human TCRα/β (clone REA652) PE	Miltenyi	Cat#130-113-539
anti-Human TCRα/β (clone REA652) APC Vio 770	Miltenyi	Cat#130-113-536
anti-Human TCRγ/δ (clone REA591) PE	Miltenyi	Cat#130-114-038
Sytox blue viability dye	Fisher sci.	Cat#10482112
Viobility 405/452 Fixable Dye	Miltenyi	Cat#130-110-205
BD HorizonTM Fixable Viability Stain 700	BD Biosciences	Cat#564997
anti-mouse TNF (clone MP6-XT22) FITC	BD Biosciences	Cat#554418
anti-mouse CD8a (clone REA601) APC Vio 770	Miltenyi	Cat#130-120-737
anti-mouse CD3E (clone MP6-XT22) BB700	BD Biosciences	Cat#566495
anti-mouse CD45 (Clone 737) Viogreen	Miltenyi	Cat#130-110-665
anti-mouse TREM1 (clone 174031) BV421	BD Biosciences	Cat#747899
anti-mouse F4/80 (clone T45-2342) APC	BD Biosciences	Cat#566787
anti-mouse NK1.1 (clone PK136) BV711	BioLegend	Cat#108745
anti-mouse Ly-6G (clone 1A8) FITC	BD Biosciences	Cat#561105
anti-mouse Ly-6C (clone 796) BB700	Miltenyi	Cat#130-111-782
anti-mouse CD11b (clone M1/70) APC Cy7	BioLegend	Cat#101226
anti-Human CD15 (clone REA1188) BV786	BD Biosciences	Cat#563838
Mouse Anti-Human HLA-DP, DQ, DR Antigen, Clone CR3/43	Agilent	Cat#M077501-2
Mouse anti Human GNLY	Abcam	Cat#ab241333
anti-mouse CD16/CD32 (clone 93)	ThermoFish. Sci.	Cat#14-0161-83
Biological Samples		
HCC and adjacent non-tumoral liver	Fresh resections from patients with informed consent for approved study. Surgeries were done by the department of Oncology, Haut Leveque Hospital, Pessac	N/A
Hep55.1C cells	CLS	Cat#400201

K562	ATCC	Cat#CCL-243
TERT-specific $CD4^+$ T cell clone	A gift from O. Adotevi	N/A
Animal Models		
C57BL/6J SFP	Charles River	Cat#632
BKS.Cg-Dock7m$^{+/+}$LeprdbJ SPF	Charles River	Cat#607
Chemicals, Peptides and recombinant Proteins		
Percoll	Sigma-Aldrich	Cat#P1644
Phorbol 12-myristate 13-acetate	Sigma-Aldrich	Cat#79346
Carbon tetrachloride	Sigma-Aldrich	Cat#319961
Olive oil	Sigma-Aldrich	Cat#O1514
Recombinant Human IL-2	Peprotech	Cat#200-02
Recombinant Human IL-15	Peprotech	Cat#200-15
Recombinant Human IL-6	Miltenyi	Cat#130-093-929
Recombinant Human GM-CSF	Miltenyi	Cat#130-093-862
Red Blood Cell Lysis Buffer	Merck	Cat#11814389001
Ionomycin	Sigma-Aldrich	Cat#I0634
GentleMACS C tubes	Miltenyi	Cat#130-096-334
Tumor Dissociation Kit, human	Miltenyi	Cat#130-095-929
Prolong Gold Antifade mountant	ThermoFicher Sci.	Cat#P36930
Fixation/Permeabilization Solution Kit with BD GolgiPlug™	BD Biosciences	Cat#555028
CellTrace CFSE	ThermoFisher sci.	Cat# C34554
RPMI Medium 1640 (1X)	GIBCO	Cat#22400071
DMEM Medium High Glucose	GIBCO	Cat#41965-09
DPBS without calcium without magnesium	Fisher Sci.	Cat#12559069
Bovine Serum Albumin Fraction V (7.5%)	Fisher Sci.	Cat#11500496
EDTA 0.5 M UltraPure™, pH 8.0	Fisher Sci.	Cat#15575020
CO2 Independent medium	Fisher Sci.	Cat# 11580536
Penicillin / Streptomycin	Fisher Sci.	Cat# 11556461
PGN-SA	Invivogen	Cat#tlrl-pgns2
rhPGLYRP1/PGRP-S	R&D system	Cat#2590-PGB-050
Propylene glycol	ThermoFish. Sci.	Cat#158720010
GF9 peptide	Genentech	GLLSKSLVF
Control peptide	Genentech	GLLSGSLVF
UCP4 TERT Peptide	Eurofin	SLCYSILKAKNAGMS

Matrigel high concentration	BD Biosciences	Cat#354262
Isopentane RE	Carlo Erba	Cat#528492
Critical Commercial Assays		
Cell strainer 40µm	Corning	Cat#431750
Cell strainer 70µm	Corning	Cat#352350
Trypan blue solution	Sigma-Aldrich	Cat#T8154
Opal 570 Fluorophore	Akoya	Cat#FP1488001KT
Opal 520 Fluorophore	Akoya	Cat#FP1487001KT
1X Plus Amplification Diluent	Akoya	Cat#FP1498A
Opal polymer HRP Ms+Rb	Akoya	Cat#ARH1001EA
Spectral DAPI solution	Akoya	Cat#FP1490A
Blocking/Ab Diluent	Akoya	Cat#ARD1001EA
10X AR6 buffer	Akoya	Cat#AR6001KT
10X AR9 buffer	Akoya	Cat#AR900250ML
Chromium i7 Multiplex Kit, 96 reactions	10x Genomics	Cat#120262
Chromium Next GEM Chip G Single Cell Kit	10x Genomics	Cat#1000120
Chromium Next GEM Single Cell 3' GEM, Library & Gel Bead Kit v3.1	10x Genomics	Cat#1000121
Bluing Buffer	Agilent	Cat#CS70230-2
Hematoxylin, Mayer's	Agilent	Cat#S30930-2
Eosin Y solution, aqueous	Merck	Cat# HT110219
Sodium dodecyl sulfate (SDS) solution, 10% in water	Merck	Cat# 71736
Visium Spatial Gene Expression Starter Kit	10x Genomics	Cat#1000200
Dual Index Kit TT Set A 96 rxns	10x Genomics	Cat#1000215
BSA Ultra Pure	Fischer Sci.	Cat#10743447
Methanol	Sigma-Aldrich	Cat#34860
Acetic Acid > 99.9%	Sigma-Aldrich	Cat#A6283
Low TE Buffer	ThermoFisher sci.	Cat#12090-015
SSC Buffer 20x Concentrate	Sigma-Aldrich	Cat#S66391L
Potassium hydroxide solution volumetric, 8.0 M KOH	Sigma-Aldrich	Cat# P4494
Hydrochloric acid solution volumetric, 0.1 M HCl, endotoxin free	Sigma-Aldrich	Cat#2104
10% Tween 20	Biorad	Cat#1662404
Tris (1 M) pH 7,0	ThermoFisher sci.	Cat#AM9850G

SPRISelect Reagent	Beckman Coulter	Cat#B23318
Eukitt® Quick-hardening mounting medium	Sigma-Aldrich	Cat#3989
Fixation/Permeabilization Solution Kit with BD GolgiPlug™	BD Biosciences	Cat#555028
CellTrace CFSE	ThermoFisher sci.	Cat# C34554
16% Formaldehyde (W/V)	Fisher sci.	Cat# 11586711
X-VIVO15 medium	Lonzo	Cat#BE02-060Q
RNeasy Minikit	Qiagen	Cat#74104
RNeasy Plus Micro Kit	Qiagen	Cat#74034
QIAshreader	Qiagen	Cat#79656
GoScriptTM reverse transcription system	Promega	Cat#A5001
GoTaq® qPCR Master Mix	Promega	Cat#A6001
O.C.T. Compound	VWR	Cat#361603E
DNA LoBinding Tubes, 1.5 mL	Eppendorf	Cat#022431021
Irradiated MCD-Diet AIN-76	SAFE	Cat#v248
Dnase I	Sigma-Aldrich	Cat#DN25
Collagenase IV	Sigma-Aldrich	Cat#C5138
Human pan T cell isolation kit	Miltenyi	Cat#130-096-535
Dynabeads human T-activator CD3/CD28	Gibco	Cat#11131D
Human $CD14^+$ cell isolation kit	Miltenyi	130-050-201
Human CXCL8/IL-8 Duoset	R&D system	Cat#DY208-05
Human IL-10 Duoset	R&D system	Cat#DY217B-05
Human sTREM1 Quantikine	R&D system	Cat#DTRM10C
CellTrace Violet system	ThermoFisher Sci.	Dye Cat# C34571
Human primers		
COL1A1	F-CCCTCCTGACGCACGG	R-GTGATTGGTGGGATGTCTT
RPL0	F-GCAGCATCTACAACCCTGA	R-CACTGGCAACATTGCGGAC
18S	F-TGCCATCACTGCCATTAAG	R-TGCTTTCCTCAACACCACAT
TGFB1	F-CTAATGGTGGAAACCCACA	R-TATCGCCAGGAATTGTTGC
Imaging System		
NanoZoomer 2.0HT	Hamamatsu	N/A
DM5500B TCS SPE	Leica	N/A
Software and Algorithms		
DIVA	BD Biosciences	https://www.bdbiosciences.com/en-fr

FlowJo v.10.5.3	FlowJo	https://www.flowjo.com
NDP View2	Hamamashu	https://www.hamamatsu.com
GraphPad Prism 9	GraphPad	https://www.graphpad.com/scientific-software/prism/
Adobe Illustrator	Adobe	www.adobe.com
CellRanger v6.0.0	10x Genomics	https://support.10xgenomics.com/single-cell-gene-expression/software/overview/welcome
SpaceRanger v1.3.0	10x Genomics	https://support.10xgenomics.com/single-cell-gene-expression/software/overview/welcome
R 4.0.0	The R core Team	https://www.r-project.org
CellTypist	Domínguez Conde et al., 2021	https://github.com/Teichlab/celltypist
BBrowser BioTuring	https://www.biorxiv.org/content/10.1101/2020.12.11.414136v1	https://bioturing.com/bbrowser
Python 3.6	Python Software Foundation	https://www.python.org
CIBERSORTx	Newman et al. 2019 (Newman et al., 2019)	https://cibersortx.stanford.edu/
CytoTRACE	Gulati et al. 2020 (Gulati et al., 2020)	https://cytotrace.stanford.edu/

2) RESOURCE AVAILABILITY

Lead Contact. Further information and requests should be directed to and will be fulfilled by the Lead Contact, Dr. Maya Saleh (maya.saleh@mac.com).

3) EXPERIMENTAL MODELS AND SUBJECT DETAILS

Patient Clinical Characteristics. Samples were collected from patients diagnosed with HCC. Among the patients used for scRNAseq, five were obese with an IMC > 30, six were diagnosed as lower stage (stages <3) and four as higher stage (stages ≥3) according to Edmondson-Stainer histopathological classification. Three patients were HCV-infected, three had NASH, three were cirrhotic and three where alcoholic. The patients detailed clinical characteristics are summarized in Table S1.

Human HCC Samples. The adjacent non-tumoral (NT) and tumoral (HCC) tissues were obtained from patients undergoing liver resection surgery at the Haut Leveque Hospital (Pessac, France) with written consent.

990 **Cell-Lines.** The K562 human cell-line was obtained from the American Type Culture
991 Collection and grown in RPMI 1640 supplemented with fetal bovine serum (FBS, 10%),
992 glutamine (1%) and penicillin/streptomycin (1%) (named complete medium). Hep55.1C
993 murine syngenic cell-line was obtained from the American Type Culture Collection and grown
994 in DMEM, high glucose, GlutaMAX™ Supplement, pyruvate (Fisher 11594446) supplemented
995 with fetal bovine serum (FBS, 10%) and penicillin/streptomycin (1%). These cell-lines were
996 grown at 37°C in a humidified chamber with 5% CO2 and regularly tested as negative for
997 mycoplasma. UCP4-specific $CD4^+$ T cells were cultured as previously reported (Dosset et al.,
998 2012).
999
1000 **Generation of HuMoSCs.** HuMoSCs were generated according to a published protocol
1001 (Janikashvili *et al.*, 2015). Briefly, healthy donor peripheral blood mononuclear cells (PBMC)
1002 were obtained from buffy coats by the means of Ficoll density gradient centrifugation.
1003 Monocytes were then isolated from PBMC by magnetic cell sorting (human $CD14^+$ cell
1004 isolation kit; Miltenyi Biotec, 130-050-201). HuMoSCs were generated by incubating
1005 monocytes (1.10^6 cells/mL) in RPMI 1640 supplemented with 10% FBS, 1% glutamine,
1006 pyruvate, Hepes, AANE and recombinant human GM-CSF (10 ng/mL; Militenyi Biotec, 130-
1007 093-862) and IL-6 (10 ng/mL; Militenyi Biotec, 130-093-929) for 7 days. Sixty percent of the
1008 medium was replaced every 3 days. PGN/PGLYRP1 complex (2 µg/mL and 1 µg/mL,
1009 respectively) or PBS were added in the HuMoSC medium on day 6 for 24 hours. sTREM1, IL-
1010 8 and IL-10 were quantified in the medium of HuMoSC cultures on day 7.
1011
1012 ***In Vivo* Animal Studies.** The mice used in this study were male C57BL/6J and BKS.Cg-
1013 *Dock7*^{m}*+/+Lepr*^{dbJ} purchased from Charles River. Mice were housed under specific pathogen-
1014 free conditions at the animal facility at Pessac (University of Bordeaux). All experimental
1015 procedures were approved by the local ethical committee in accordance with the regulations of
1016 the French ministry.

1017 **4) EXPERIMENTAL METHODS**

1018
1019 **Fibrosis and NASH mouse models.** Liver fibrosis was induced in 6-week-old C57BL/6J male
1020 mice with intraperitoneal (i.p.) injection of CCL4 at the dose of 2µl/g body weight diluted 1:19
1021 in olive oil, twice a week for 10 weeks. Adult 8-week-old male db/db mice were fed a
1022 Methionine- and Choline-Deficient diet (MCD-diet) from week 8 to week 16. The diet was
1023 halted 9 days between weeks 11.3 and 12.7. Comparison was made to age-matched olive-oil
1024 treated mice (controls, i.p. injection) and mice were sacrificed at 16-weeks of age.
1025
1026 **Mouse liver dissociation.** Mouse liver was dissociated in Gentle MACS C tubes containing
1027 RPMI medium supplemented by 1% glutamine, 1% P/S, 50 µl/mL DNAse I and 1 mg/mL
1028 collagenase IV for 45 minutes at 37°C under agitation. C tubes were run in GentleMACS
1029 dissociator before and after incubation (program mLiver_3, Miltenyi). After a first step of
1030 centrifugation at 400 xg for 8 min at 4°C, dissociated cells were passed through a 70 µm filter,
1031 rinsed with complete RPMI and centrifuged at 400 xg for 5 min at 4°C. After a treatment with
1032 5 mL red blood cell lysis (Roche) at 4°C for 5 minutes, cells were washed twice with PBS 2
1033 mM EDTA 0.1% BSA (named FACS buffer) and viable immune cells were enriched in a
1034 40:80% Percoll® gradient.
1035

1036 **Human tissue dissociation.** The tissues were collected in CO_2 independent medium (Fisher
1037 sci., Cat# 11580536) and kept on ice until processing within one hour. One piece was placed in
1038 RNA later and conserved at -80°C until RNA extraction. One histological slice was fixed in
1039 10% buffered formalin phosphate (Sigma) and paraffin-embedded. HES-stained slides were
1040 reviewed by a pathologist (Figure S1). The other slice was embedded in OCT (VWR) and put
1041 in a bath of isopentane placed in a liquid nitrogen bath. The OCT-embedded tissue blocks were
1042 stored in a sealed container at -80°C until cryo-sectioning. The last tissue was rinsed in RPMI,
1043 transferred to a sterile 60 mm^2 tissue culture dish and cut in 1 mm^3 pieces. Tissue pieces were
1044 placed in Gentle MACS C tubes and incubated in tissue dissociation solution (tumor
1045 dissociation kit, Miltenyi) using the GentleMACS dissociator (program h_TDK_2, Miltenyi).
1046 After a first step of centrifugation at 400 xg for 8 min at 4°C, dissociated cells were passed
1047 through a 40 µm filter, rinsed with complete RPMI and centrifuged at 400 xg for 5 min at 4°C.
1048 After a treatment with 5 mL red blood cell lysis (Roche) at 4°C for 5 minutes, cells were washed
1049 twice with PBS 2 mM EDTA 0.1% BSA (named FACS buffer) prior to counting in Trypan
1050 blue exclusion dye.
1051
1052 **Flow cytometry staining.** Dissociated cells were incubated with cell surface antibodies in
1053 FACS buffer for 25 minutes at 4°C in the dark or for 15 munites at room temperature and
1054 washed twice before analysis. For intracellular staining of cytokines, cells were fixed and
1055 permeabilized with Fixation/Permeabilization Solution Kit according to manufacturer
1056 instructions (BD Biosciences). Viable cells were analyzed based on side scatter and viability
1057 dye. Analysis was performed on the BD LSRFortessa. Cells from murine samples were blocked
1058 in anti-mouse CD16/32 antibody (1:200e) for 10 min at 4°C prior to addition of cell surface
1059 antibodies.
1060
1061 **Single-cell FACS sorting.** For scRNAseq experiments, freshly dissociated single-cell
1062 suspensions were sorted based on this gating: FITC-CD45 $^{+}$, APC.Cy7-panTCRαβ^{-} and
1063 PE.Cy7-CD19^{-} cells. For the cytotoxicity experiments, freshly dissociated single-cell
1064 suspensions from non-tumoral liver were sorted based on this gating: Viogreen-CD45^{+}, AF700-
1065 CD19^{-}, PE-panTCRαβ^{-}, PE-panTCRγδ^{-} and APC-CD94$^{+/-}$ FITC-HLA-DR$^{+/-}$ or Viobright 515-
1066 CD56^{+}. For the immunosuppression experiments, dissociated tumor single-cell suspensions
1067 were thawed in complete RPMI medium and incubated for 10 minutes at 37 °C to wash out
1068 residual DMSO in media. Cells were pelleted and suspended in cold FACS buffer prior to
1069 staining with cell surface antibodies: Viogreen-CD45^{+} APC Vio 770-Lin^{-} (CD3, CD19, CD56)
1070 FITC-CD36^{+} PE.Cy7-CD163$^{+/-}$ APC-LOX-1$^{+/-}$.Viable cells were analyzed based on side scatter
1071 gates and Sytox blue viability dye 1:5000 (Miltenyi). Cells were sorted using FACS Aria II at
1072 4°C in pre-coated (2 hours at 37°C with PBS 10% FCS) 1.5 mL low binding tubes (Eppendorf)
1073 containing either PBS-0.04% pure BSA (for scRNAseq experiments) or complete RPMI (for
1074 co-culture experiments). Sorted cells were centrifuged 350 xg at 4°C for 5 minutes and counted
1075 with trypan blue dye before being processed.
1076
1077 **Single cell RNA sequencing Experiment.** 15.000 single CD45+ panTCRαβ- CD19- innate
1078 immunity cells were loaded into a chip to form Gel Bead-in-Emulsion in the Chromium
1079 Controller. Single-cell libraries were generated using the Single Cell 3' reagent Kit v3.1 (10X
1080 Genomics) as per the manufacturer's protocol. cDNA was amplified by 12 PCR cycles and 12
1081 cycles were also performed for library preparation (single index PCR). Libraries were pooled
1082 and sequenced on a NovaSeq 6000.
1083

1084 **Visium Spatial gene expression Processing.** OCT-embedded tissue blocks were sectioned at
1085 10 µm thickness using Cryostar NX70 (Leica) and tumoral tissues containing RNA with a RIN
1086 ≥ 6.8 were included in the Visium experiments. One section per patient was cut at 10 µm
1087 thickness and placed on Visium slide capture areas (10x Genomics). Slides were then processed
1088 following the 10x Genomics Visium Spatial protocol according to the manufacturer
1089 recommendations. The slides containing tissues were methanol-fixed at -20°C and processed
1090 for H&E staining and imaging. The slides were scanned using a Nanozoomer 2.0HT
1091 (Hamamatsu Photonics France) using objective UPS APO 20X NA 0.75 combined with an
1092 additional lens 1.75X. Virtual slides were acquired with a TDI-3CCD camera. Based on tissue
1093 optimization experiments performed on HCC#20, HCC tissues were permeabilized for 12
1094 minutes. cDNA was amplified by 14 PCR cycles and 14 cycles were also performed for library
1095 preparation (dual index PCR). Libraries were pooled and sequenced on a NovaSeq 6000.
1096
1097 **Multiplexed Immunohistological Staining and Imaging.** 3.5µm-thick formalin-fixed
1098 paraffin-embedded tissue sections were placed at 37°C overnight and then for 1h at 56°C. The
1099 slides were then deparaffinized in fresh xylene and rehydrated in decreasing concentrations of
1100 ethanol. The slides were immersed in AR9 buffer, placed in a jar and heated in a microwave
1101 for 90 sec at 1000 mw until the buffer boils, followed by an additional microwave treatment for
1102 15 minutes at 160 mw. Slides were allowed to cool down for 20 minutes at room temperature,
1103 rinsed with distilled water and then in Tris-Buffered Saline Tween 0.05 (v/v) (TBST) and
1104 blocked in antibody diluent / Block (Akoya) for 10 minutes at room temperature. After primary
1105 antibody incubation (HLA-DR, 1:400e 1 hour at 37°C) and washing in TBST, secondary-HRP
1106 solution was applied onto the slides for 10 minutes at room temperature. After washing in
1107 TBST, Opal 520 (Akoya, 1:100e) solution was applied on each slide at room temperature for
1108 10 minutes. Next, slides were rinsed in TBST and placed in AR9 buffer to perform a second
1109 cycle of microwave treatment, blocking, primary antibody incubation (GNLY, 1:1000e
1110 overnight at 4°C) and Opal 570 deposition (Akoya, 1:100e). At the end of the cycle, slides were
1111 counterstained with spectral DAPI (Akoya) and mounted with Prolong Antifade Mountant
1112 (Thermofisher sci.). The microscopy was done in the Bordeaux Imaging Center, a service unit
1113 of the CNRS-INSERM and Bordeaux University, member of the national infrastructure France
1114 BioImaging supported by the French National Research Agency (ANR-10-INBS-04). The
1115 confocal images were taken using objectives ACS APO 40X oil NA 1.15 and the lasers used
1116 were diodes laser (405 nm, 488 nm and 561 nm).
1117
1118 **Co-culture experiments.** *For the cytotoxicity experiments*, freshly sorted cells were incubated
1119 for 12-14h in round bottom 96-well plates with CFSE-labeled K562 cells at a ratio 5:1 in
1120 complete RPMI. Briefly, 1 million K562 cells were incubated with 1 µM CellTrace CFSE dye
1121 (ThermoFisher sci.) for 20 minutes at 37°C, cells were then incubated 7 minutes at room
1122 temperature with complete RPMI and centrifuged prior to seeding with sorted cells. Cells were
1123 simulated or not with IL-2 (Peprotech, 20 ng/ mL) and IL-15 (Peprotech, 50 ng/mL). At the end
1124 of the co-culture time, Sytox blue was added to the medium (1:5000) and K562-CFSE+ dead
1125 cells were quantified using LSRFortessa. *For the immunosuppression experiments with*
1126 *patients-derived MDSCs*, MDSC cells sorted from HCC surgical resections were pre-incubated
1127 for 4 hours in round bottom 96-well plates with a TERT-reactive $CD4^+$ T lymphocyte clone at
1128 a ratio of 5:1 and then stimulated for 12 hours with UCP4 TERT peptides plus BD Golgi Plug
1129 each at 1µg/mL final concentration. For the control, T cells were stimulated with Phorbol 12-
1130 myristate 13-acetate at 50 ng/mL and ionomycin at 2 µg/mL (Sigma). *For the*
1131 *immunosuppression experiments with HuMoScs,* total T lymphocytes were purified from
1132 healthy donor PBMC from buffy coats by the means of magnetic cell sorting using human pan

1133 T-cell isolation kits according to manufacturer's procedure (Militenyi Biotec; 130-096-535).
1134 The obtained T-cells were then activated with anti-CD3/CD28-coated beads (Dynabeads, Life
1135 Technologies, 11131D) with or without HuMoSCs at different ratios (T-cell/ HuMoSC ratio =
1136 1:1, 1:4). In both immunosuppression tests, cells were pelleted and suspended in FACS buffer
1137 prior to staining with cell surface antibodies (CD4-PE C7 and CD3-APC-Vio770) solution
1138 containing fixable viability dye. After washing, fixation and permeabilization, intracellular
1139 staining with antibody against IFNγ-APC and TNFα□FITC was performed using BD
1140 fixation/Permeabilization solutions as per the manufacturer's recommendations (BD
1141 Biosciences). The % inhibition of T cell activity was calculated as: [(% IFNγ^+ CD4$^+$ T cell or
1142 TNFα^+ CD4$^+$ T cell in the positive control stimulation i.e. with the TERT-derived peptide or
1143 with anti-CD3/CD28 antibodies) − (% IFNγ^+ CD4$^+$ T cell or TNFα^+ CD4$^+$ T cell in the other
1144 tested wells) × 100]/(% IFNγ^+ CD4$^+$ T cell or TNFα^+ CD4$^+$ T cell in the positive control
1145 stimulation). In the proliferation assay, T cells were stained with CellTrace Violet Dye
1146 (ThermoFisher sci. Cat# C34571) according to the manufacturer's recommendations and then
1147 activated with anti-CD3/CD28-coated beads with or without HuMoSCs (ratio 1:1). After 6 days
1148 of co-culture, proliferation of CD3$^+$ T cells was analyzed by flow cytometry.
1149
1150 **Orthotopic tumor injection and tumor growth monitoring.** 10-week old C57BL/6J male
1151 mice were treated with buprenorphine s.c. at 0.1mg/kg 30 min prior to anesthesia with
1152 isoflurane (2 L/min oxygen). Laparotomy was done to expose the left lateral liver lobe and 20
1153 µL of Hep55.1C cells (0.25 x 10^6 cells) /Matrigel (7 mg/mL) suspension was gently injected
1154 under the liver capsule. A sterile Gel foam was placed on the needle track for 2 min to prevent
1155 leakage of cells. Mice were treated with GF9 or control peptides at 25 mg/kg (in 20% propylene
1156 glycol, 10% ethanol and 2% Tween 80, i.p. injection) three times a week from day 7 post
1157 inoculation of cells till day 21. Tumor growth was monitored using bioluminescence on
1158 isoflurane anesthetized mice.
1159
1160
1161 **5) BIOINFORMATICS METHODS**
1162
1163 **Single-cell RNA-Seq data processing, quality control and cleaning.** A data processing
1164 summary is presented in Figure S1c and Table S7. Each of the 10X Chromium single-cell Gene
1165 Expression data were pre-processed using CellRanger software 6.0.0, including
1166 demultiplexing, reads alignment on human reference genome assembly GRCh38 (refdata-gex-
1167 GRCh38-2020-A), barcoding and counting of unique UMI. Raw UMI count matrices were
1168 imported in R environment to perform deeper quality control steps to exclude low-quality cells.
1169 Cells containing less than 300 or more than 4,500 detected features and cells with more than
1170 40,000 counts were discarded. Moreover, cells expressing more than 12% of mitochondrial
1171 genes or more than 15% of ribosomal genes were eliminated. A supplementary criteria was
1172 added to exclude stressed cells based on a stress response score(Denisenko et al., 2020). The
1173 stress response score was calculated using *AddModuleScore* function from Seurat package
1174 (version 4.0.1), and the following list of genes: *FOSB, FOS, JUN, JUNB, JUND, ATF3, EGR1,*
1175 *HSPA1A, HSPA1B, HSP90AB1, HSPA8, HSPB1, IER3, IER2, BTG1, BTG2, DUSP1*.
1176
1177 **Cell doublet detection and removal.** Three different doublet predictions were performed using
1178 DoubletFinder (version 2.0.3) (McGinnis et al., 2019), scDblFinder (version 1.7.7) (Germain
1179 et al., 2021) and scds (version 1.8.0) (Bais and Kostka, 2020). A consensus method was applied,
1180 i.e. a cell was considered as a multiplet and discarded if identified in at least two of the three
1181 methods. On average, doublets were estimated around 4%, ranging from 1% (sample with the

lowest number of cells) to 5.8%. Cleaning and doublets removal account for 10 to 47% of the cells retrieved with CellRanger. Total recovery ranges from 11 to 49% (Suppl. Table 6).

Normalization and Data Integration. The 20 pre-processed scRNA-seq data (10 adjacent non-tumoral and 10 tumoral) were normalized using SCTransform (version 0.3.2) with method = «glmGamPoi» before integration. Functions *PrepSCTIntegration* with 3,000 features, *FindIntegrationAnchors* with dims = 30, reduction = «rpca» and reference (4 samples) options, and *IntegrateData* from Seurat were used to integrate all 20 samples.

Unsupervised clustering, dimensionality reduction and Data Visualization. Unsupervised clustering, dimensionality reduction and most visualization were performed with Seurat (version 4.0.1). RunPCA function was used with 30 dimensions. The optimized number of dimensions used for RunTSNE and RunUMAP functions was automatically calculated with an in-house script. *FindNeighbors* and *FindClusters* (res=0.5) function were used to predict the 22 clusters described in the main text. *FindAllMarkers* (min.pct = 0.25, logfc.threshold = 0.25) function was used to identify discriminating features between clusters.

Cell type/state annotation. Automatic and manual methods were combined to annotate as precisely as possible cell types or states: (1) expression of canonical markers were visualized and lists of discriminating markers were first manually investigated; (2) lists of markers were downloaded from Panglao database, a score method was applied using AddModuleScore and results were visualized on FeaturePlots; and (3) automatic predictions were done using CellTypist (Domínguez Conde et al., 2021) with the whole dataset and cellKB software (Patil and Patil, 2022) using discriminating lists of markers as input.

Identification of signature genes. We defined gene signatures as the minimal number of genes allowing to discriminate a cluster from others. Top 20 discriminating genes were investigated and adjusted as necessary to refine the signatures. To validate signatures, scores were calculated using *AddModuleScore* and visualized using *VlnPlot* and *FeaturePlot* functions from Seurat on the different sets. Signature specificity was calculated as the mean expression of a marker gene in a test cluster divided by the mean expression of the same gene in the cluster that expresses it at its second highest level.

Trajectory Inference. Trajectory analyses were performed using monocle (version 2.20.0) and slingshot (version 1.6.1) R packages. A reduced number of cells (n = 300) was used to increase the speed of calculation using subset function from Seurat option downsample. Differentially and temporally expressed genes were identified using differentialGeneTest function with options fullModelFormulaStr = '~Cluster' and fullModelFormulaStr = "~sm.ns(Pseudotime)", respectively.

Estimation of differentiation potency or signaling entropy. The differentiation potency of single-cells was estimated using the SCENT package (Teschendorff and Enver, 2017), with the provided functional gene network «net13Jun12». Normalized count matrices were log(x + 1) transformed. Signaling Entropy Rates (SR) were calculated using Correlation of Connectome and Transcriptome (CCAT) (Teschendorff et al., 2021) with CompCCAT function, implemented in SCENT. High values indicate higher potency or signaling promiscuity/entropy (capacity to differentiate to different lineages). Furthermore, we predicted differentiation states using CytoTRACE (Gulati et al., 2020). We downsampled MNP sets by using 200 cells per cluster and used the online version of CytoTRACE.

Differential Expression Analysis, Gene Ontology and Gene Set Enrichment Analysis. Differential gene expression between two clusters or between two conditions were performed using *FindMarkers* function from Seurat. Gene Ontology analyses were done using topGO (version 2.44.0) and org.Hs.eg.db (version 3.13.0) R packages.

Pre-processing and visualization of spatial transcriptomic data. Spatial data were pre-processed and aligned using SpaceRanger software v1.3.0 with the reference human genome GRCh38 (refdata-gex-GRCh38-2020-A) to generate raw UMI count spot matrices. Raw UMI counts were normalized using SCTransform. Dimensionality reduction was performed using classical PCA and clustering was performed using Louvain clustering with *FindNeighbors* and *FindClusters* functions, as before. Signatures were spatially visualized using *AddModuleScore* function. Gene expression visualizations were generated using BBrowser BioTuring (Le *et al.* BioRxiv).

Transcriptomic source data of external cohorts. To validate the tissue distribution of MNP subsets and their association with clinical parameters, we interrogated several large cohorts of patients with HCC and other solid tumors. First, to validate the enrichment or depletion of cell types, we compared Non Tumoral (NT) and Primary Solid Tumor (T) samples from five different TCGA cohorts: LIHC, KIRC, LUAD, COAD and READ (https://www.cancer.gov/tcga). Normalized count tables were downloaded using TCGAbiolinks R package (Colaprico et al., 2016) with GDCquery function and the following options : data.category = «Gene expression», data.type = «Gene expression quantification», platform = «Illumina HiSeq», file.type = «normalized_results». Clinical data with patient overall survival durations and tumor grades were downloaded with the GDCquery_clinic function. Supplementary clinical information of 196 patients of the LIHC cohort were retrieved from The Cancer Genome Atlas Research Network (Cancer Genome Atlas Research Network. Electronic address and Cancer Genome Atlas Research, 2017). We also tested MNP subsets associations with patient response to anti-PD-1 in ccRCC (Braun *et al.*, 2020), and in metastatic melanoma (Hugo *et al.*, 2017).

1261 **Immuno-deconvolution and cancer genomics.** We estimated proportions of scRNA-seq cell
1262 subsets in the previously cited external cohorts using CIBERSORTx (Steen *et al.*, 2020). We
1263 used our MNP set and a second scRNA-seq set containing 58 cell populations including
1264 fibroblasts, stromal cells and adaptive immune cells (Qi et al., 2022). To extract the normalized
1265 count matrix, we downsampled the number of barcodes per cell type to 200 for our MNP subsets
1266 and 100 cells per cell type for the set from Qi *et al.* (Qi et al., 2022). We built scRNA-seq
1267 signature matrices in CIBERSORTx web server. We imputed cell fractions of each immune set
1268 within each cohort described in the previous section, with option S-mode 'Batch correction'.
1269 Parsing and visualizations of the proportions were then realized using tidyverse, reshape2,
1270 ggplot2, ggsignif, pheatmap, cowplot and corrplot R packages. We performed survival analyses
1271 using survminer and survival R packages. Moreover, we verified CIBERSORTx signatures for
1272 each cell-type based on signature scoring from file 'sig_inferred_refsample.bm.K999.txt'. We
1273 extracted top-scored 100 genes per cluster. This allowed us to validate our manual signatures
1274 to identify highly specific genes.

1275 **6) STATISTICAL ANALYSES**

1276 Statistical analyses were performed with GraphPad Prism version 9 (GraphPad software) or R
1277 version 4.1. The statistical tests used are reported in the Figure Legends. LogFC T/NT ratios
1278 were calculated as the Log (cell number in the tumor *RCF + 1) – Log (cell number in the non-
1279 tumoral tissue *RCF +1) with RCF corresponding to the recovered cell number in either tissue.
1280 Cell abundance correlations were calculated using corrplot (version 0.92) and Hmisc (version
1281 4.6.0) R packages. Correlation matrix was done using *cor* function with pearson method and
1282 corrplots were calculated using options order="hclust".

1283 **References**

1284

1285 Blasius, A.L., Barchet, W., Cella, M., and Colonna, M. (2007). Development and function of
1286 murine B220+CD11c+NK1.1+ cells identify them as a subset of NK cells. J Exp Med *204*,
1287 2561-2568. 10.1084/jem.20070991.
1288 Bouchon, A., Facchetti, F., Weigand, M.A., and Colonna, M. (2001). TREM-1 amplifies
1289 inflammation and is a crucial mediator of septic shock. Nature *410*, 1103-1107.
1290 10.1038/35074114.
1291 Braun, D.A., Hou, Y., Bakouny, Z., Ficial, M., Sant' Angelo, M., Forman, J., Ross-Macdonald,
1292 P., Berger, A.C., Jegede, O.A., Elagina, L., et al. (2020). Interplay of somatic alterations and
1293 immune infiltration modulates response to PD-1 blockade in advanced clear cell renal cell
1294 carcinoma. Nat Med *26*, 909-918. 10.1038/s41591-020-0839-y.
1295 Caminschi, I., Ahmet, F., Heger, K., Brady, J., Nutt, S.L., Vremec, D., Pietersz, S., Lahoud,
1296 M.H., Schofield, L., Hansen, D.S., et al. (2007). Putative IKDCs are functionally and
1297 developmentally similar to natural killer cells, but not to dendritic cells. J Exp Med *204*, 2579-
1298 2590. 10.1084/jem.20071351.
1299 Cancer Genome Atlas Research Network. Electronic address, w.b.e., and Cancer Genome Atlas
1300 Research, N. (2017). Comprehensive and Integrative Genomic Characterization of
1301 Hepatocellular Carcinoma. Cell *169*, 1327-1341 e1323. 10.1016/j.cell.2017.05.046.
1302 Chan, C.W., Crafton, E., Fan, H.N., Flook, J., Yoshimura, K., Skarica, M., Brockstedt, D.,
1303 Dubensky, T.W., Stins, M.F., Lanier, L.L., et al. (2006). Interferon-producing killer dendritic
1304 cells provide a link between innate and adaptive immunity. Nat Med *12*, 207-213.
1305 10.1038/nm1352.
1306 Chiaramonte, M.G., Donaldson, D.D., Cheever, A.W., and Wynn, T.A. (1999). An IL-13
1307 inhibitor blocks the development of hepatic fibrosis during a T-helper type 2-dominated
1308 inflammatory response. J Clin Invest *104*, 777-785. 10.1172/JCI7325.
1309 Colaprico, A., Silva, T.C., Olsen, C., Garofano, L., Cava, C., Garolini, D., Sabedot, T.S., Malta,
1310 T.M., Pagnotta, S.M., Castiglioni, I., et al. (2016). TCGAbiolinks: an R/Bioconductor package
1311 for integrative analysis of TCGA data. Nucleic Acids Res *44*, e71. 10.1093/nar/gkv1507.
1312 Condamine, T., Dominguez, G.A., Youn, J.I., Kossenkov, A.V., Mony, S., Alicea-Torres, K.,
1313 Tcyganov, E., Hashimoto, A., Nefedova, Y., Lin, C., et al. (2016). Lectin-type oxidized LDL
1314 receptor-1 distinguishes population of human polymorphonuclear myeloid-derived suppressor
1315 cells in cancer patients. Sci Immunol *1*. 10.1126/sciimmunol.aaf8943.
1316 Davidson, S., Coles, M., Thomas, T., Kollias, G., Ludewig, B., Turley, S., Brenner, M., and
1317 Buckley, C.D. (2021). Fibroblasts as immune regulators in infection, inflammation and cancer.
1318 Nat Rev Immunol *21*, 704-717. 10.1038/s41577-021-00540-z.
1319 Dosset, M., Godet, Y., Vauchy, C., Beziaud, L., Lone, Y.C., Sedlik, C., Liard, C., Levionnois,
1320 E., Clerc, B., Sandoval, F., et al. (2012). Universal cancer peptide-based therapeutic vaccine
1321 breaks tolerance against telomerase and eradicates established tumor. Clin Cancer Res *18*,
1322 6284-6295. 10.1158/1078-0432.CCR-12-0896.
1323 Duan, M., Wang, Z.C., Wang, X.Y., Shi, J.Y., Yang, L.X., Ding, Z.B., Gao, Q., Zhou, J., and
1324 Fan, J. (2015). TREM-1, an inflammatory modulator, is expressed in hepatocellular carcinoma
1325 cells and significantly promotes tumor progression. Ann Surg Oncol *22*, 3121-3129.
1326 10.1245/s10434-014-4191-7.
1327 Farrell, G., Schattenberg, J.M., Leclercq, I., Yeh, M.M., Goldin, R., Teoh, N., and Schuppan,
1328 D. (2019). Mouse Models of Nonalcoholic Steatohepatitis: Toward Optimization of Their
1329 Relevance to Human Nonalcoholic Steatohepatitis. Hepatology *69*, 2241-2257.
1330 10.1002/hep.30333.

1331 Fichtner-Feigl, S., Strober, W., Kawakami, K., Puri, R.K., and Kitani, A. (2006). IL-13
1332 signaling through the IL-13alpha2 receptor is involved in induction of TGF-beta1 production
1333 and fibrosis. Nat Med *12*, 99-106. 10.1038/nm1332.
1334 Finn, R.S., Qin, S., Ikeda, M., Galle, P.R., Ducreux, M., Kim, T.Y., Kudo, M., Breder, V.,
1335 Merle, P., Kaseb, A.O., et al. (2020). Atezolizumab plus Bevacizumab in Unresectable
1336 Hepatocellular Carcinoma. N Engl J Med *382*, 1894-1905. 10.1056/NEJMoa1915745.
1337 Gieseck, R.L., 3rd, Ramalingam, T.R., Hart, K.M., Vannella, K.M., Cantu, D.A., Lu, W.Y.,
1338 Ferreira-Gonzalez, S., Forbes, S.J., Vallier, L., and Wynn, T.A. (2016). Interleukin-13
1339 Activates Distinct Cellular Pathways Leading to Ductular Reaction, Steatosis, and Fibrosis.
1340 Immunity *45*, 145-158. 10.1016/j.immuni.2016.06.009.
1341 Giraud, J., Chalopin, D., Blanc, J.F., and Saleh, M. (2021). Hepatocellular Carcinoma Immune
1342 Landscape and the Potential of Immunotherapies. Front Immunol *12*, 655697.
1343 10.3389/fimmu.2021.655697.
1344 Goswami, S., Anandhan, S., Raychaudhuri, D., and Sharma, P. (2022). Myeloid cell-targeted
1345 therapies for solid tumours. Nat Rev Immunol. 10.1038/s41577-022-00737-w.
1346 Grinchuk, O.V., Yenamandra, S.P., Iyer, R., Singh, M., Lee, H.K., Lim, K.H., Chow, P.K., and
1347 Kuznetsov, V.A. (2018). Tumor-adjacent tissue co-expression profile analysis reveals pro-
1348 oncogenic ribosomal gene signature for prognosis of resectable hepatocellular carcinoma. Mol
1349 Oncol *12*, 89-113. 10.1002/1878-0261.12153.
1350 Guimont-Desrochers, F., Boucher, G., Dong, Z., Dupuis, M., Veillette, A., and Lesage, S.
1351 (2012). Redefining interferon-producing killer dendritic cells as a novel intermediate in NK-
1352 cell differentiation. Blood *119*, 4349-4357. 10.1182/blood-2011-11-395954.
1353 Guimont-Desrochers, F., and Lesage, S. (2013). Revisiting the Prominent Anti-Tumoral
1354 Potential of Pre-mNK Cells. Front Immunol *4*, 446. 10.3389/fimmu.2013.00446.
1355 Gulati, G.S., Sikandar, S.S., Wesche, D.J., Manjunath, A., Bharadwaj, A., Berger, M.J., Ilagan,
1356 F., Kuo, A.H., Hsieh, R.W., Cai, S., et al. (2020). Single-cell transcriptional diversity is a
1357 hallmark of developmental potential. Science *367*, 405-411. 10.1126/science.aax0249.
1358 Halaby, M.J., Hezaveh, K., Lamorte, S., Ciudad, M.T., Kloetgen, A., MacLeod, B.L., Guo, M.,
1359 Chakravarthy, A., Medina, T.D.S., Ugel, S., et al. (2019). GCN2 drives macrophage and MDSC
1360 function and immunosuppression in the tumor microenvironment. Sci Immunol *4*.
1361 10.1126/sciimmunol.aax8189.
1362 Hegde, S., Leader, A.M., and Merad, M. (2021). MDSC: Markers, development, states, and
1363 unaddressed complexity. Immunity *54*, 875-884. 10.1016/j.immuni.2021.04.004.
1364 Heinrich, B., Gertz, E.M., Schaffer, A.A., Craig, A., Ruf, B., Subramanyam, V., McVey, J.C.,
1365 Diggs, L.P., Heinrich, S., Rosato, U., et al. (2021). The tumour microenvironment shapes innate
1366 lymphoid cells in patients with hepatocellular carcinoma. Gut. 10.1136/gutjnl-2021-325288.
1367 Hellerbrand, C., Stefanovic, B., Giordano, F., Burchardt, E.R., and Brenner, D.A. (1999). The
1368 role of TGFbeta1 in initiating hepatic stellate cell activation in vivo. J Hepatol *30*, 77-87.
1369 10.1016/s0168-8278(99)80010-5.
1370 Hoshida, Y., Nijman, S.M., Kobayashi, M., Chan, J.A., Brunet, J.P., Chiang, D.Y., Villanueva,
1371 A., Newell, P., Ikeda, K., Hashimoto, M., et al. (2009). Integrative transcriptome analysis
1372 reveals common molecular subclasses of human hepatocellular carcinoma. Cancer Res *69*,
1373 7385-7392. 10.1158/0008-5472.CAN-09-1089.
1374 Howard, J., Loizon, S., Tyler, C.J., Duluc, D., Moser, B., Mechain, M., Duvignaud, A., Malvy,
1375 D., Troye-Blomberg, M., Moreau, J.F., et al. (2017). The Antigen-Presenting Potential of
1376 Vgamma9Vdelta2 T Cells During Plasmodium falciparum Blood-Stage Infection. J Infect Dis
1377 *215*, 1569-1579. 10.1093/infdis/jix149.
1378 Hugo, W., Zaretsky, J.M., Sun, L., Song, C., Moreno, B.H., Hu-Lieskovan, S., Berent-Maoz,
1379 B., Pang, J., Chmielowski, B., Cherry, G., et al. (2017). Genomic and Transcriptomic Features

of Response to Anti-PD-1 Therapy in Metastatic Melanoma. Cell *168*, 542. 10.1016/j.cell.2017.01.010.

Janikashvili, N., Trad, M., Gautheron, A., Samson, M., Lamarthee, B., Bonnefoy, F., Lemaire-Ewing, S., Ciudad, M., Rekhviashvili, K., Seaphanh, F., et al. (2015). Human monocyte-derived suppressor cells control graft-versus-host disease by inducing regulatory forkhead box protein 3-positive CD8+ T lymphocytes. J Allergy Clin Immunol *135*, 1614-1624 e1614. 10.1016/j.jaci.2014.12.1868.

Kaviratne, M., Hesse, M., Leusink, M., Cheever, A.W., Davies, S.J., McKerrow, J.H., Wakefield, L.M., Letterio, J.J., and Wynn, T.A. (2004). IL-13 activates a mechanism of tissue fibrosis that is completely TGF-beta independent. J Immunol *173*, 4020-4029. 10.4049/jimmunol.173.6.4020.

Kieffer, Y., Hocine, H.R., Gentric, G., Pelon, F., Bernard, C., Bourachot, B., Lameiras, S., Albergante, L., Bonneau, C., Guyard, A., et al. (2020). Single-Cell Analysis Reveals Fibroblast Clusters Linked to Immunotherapy Resistance in Cancer. Cancer Discov *10*, 1330-1351. 10.1158/2159-8290.CD-19-1384.

Lauret Marie Joseph, E., Laheurte, C., Jary, M., Boullerot, L., Asgarov, K., Gravelin, E., Bouard, A., Rangan, L., Dosset, M., Borg, C., and Adotevi, O. (2020). Immunoregulation and Clinical Implications of ANGPT2/TIE2(+) M-MDSC Signature in Non-Small Cell Lung Cancer. Cancer Immunol Res *8*, 268-279. 10.1158/2326-6066.CIR-19-0326.

Lee, C.G., Homer, R.J., Zhu, Z., Lanone, S., Wang, X., Koteliansky, V., Shipley, J.M., Gotwals, P., Noble, P., Chen, Q., et al. (2001). Interleukin-13 induces tissue fibrosis by selectively stimulating and activating transforming growth factor beta(1). J Exp Med *194*, 809-821. 10.1084/jem.194.6.809.

Liao, R., Sun, T.W., Yi, Y., Wu, H., Li, Y.W., Wang, J.X., Zhou, J., Shi, Y.H., Cheng, Y.F., Qiu, S.J., and Fan, J. (2012). Expression of TREM-1 in hepatic stellate cells and prognostic value in hepatitis B-related hepatocellular carcinoma. Cancer Sci *103*, 984-992. 10.1111/j.1349-7006.2012.02273.x.

Llovet, J.M., Kelley, R.K., Villanueva, A., Singal, A.G., Pikarsky, E., Roayaie, S., Lencioni, R., Koike, K., Zucman-Rossi, J., and Finn, R.S. (2021). Hepatocellular carcinoma. Nat Rev Dis Primers *7*, 6. 10.1038/s41572-020-00240-3.

Loftus, T.J., Mohr, A.M., and Moldawer, L.L. (2018). Dysregulated myelopoiesis and hematopoietic function following acute physiologic insult. Curr Opin Hematol *25*, 37-43. 10.1097/MOH.0000000000000395.

Ma, L., Hernandez, M.O., Zhao, Y., Mehta, M., Tran, B., Kelly, M., Rae, Z., Hernandez, J.M., Davis, J.L., Martin, S.P., et al. (2019). Tumor Cell Biodiversity Drives Microenvironmental Reprogramming in Liver Cancer. Cancer Cell *36*, 418-430 e416. 10.1016/j.ccell.2019.08.007.

Ma, L., Wang, L., Khatib, S.A., Chang, C.W., Heinrich, S., Dominguez, D.A., Forgues, M., Candia, J., Hernandez, M.O., Kelly, M., et al. (2021). Single-cell atlas of tumor cell evolution in response to therapy in hepatocellular carcinoma and intrahepatic cholangiocarcinoma. J Hepatol *75*, 1397-1408. 10.1016/j.jhep.2021.06.028.

Maier, B., Leader, A.M., Chen, S.T., Tung, N., Chang, C., LeBerichel, J., Chudnovskiy, A., Maskey, S., Walker, L., Finnigan, J.P., et al. (2020). A conserved dendritic-cell regulatory program limits antitumour immunity. Nature *580*, 257-262. 10.1038/s41586-020-2134-y.

Mariathasan, S., Turley, S.J., Nickles, D., Castiglioni, A., Yuen, K., Wang, Y., Kadel, E.E., III, Koeppen, H., Astarita, J.L., Cubas, R., et al. (2018). TGFbeta attenuates tumour response to PD-L1 blockade by contributing to exclusion of T cells. Nature *554*, 544-548. 10.1038/nature25501.

1427 Menyhart, O., Nagy, A., and Gyorffy, B. (2018). Determining consistent prognostic biomarkers
1428 of overall survival and vascular invasion in hepatocellular carcinoma. R Soc Open Sci *5*,
1429 181006. 10.1098/rsos.181006.
1430 Miller, J.C., Brown, B.D., Shay, T., Gautier, E.L., Jojic, V., Cohain, A., Pandey, G., Leboeuf,
1431 M., Elpek, K.G., Helft, J., et al. (2012). Deciphering the transcriptional network of the dendritic
1432 cell lineage. Nat Immunol *13*, 888-899. 10.1038/ni.2370.
1433 Mulder, W.J.M., Ochando, J., Joosten, L.A.B., Fayad, Z.A., and Netea, M.G. (2019).
1434 Therapeutic targeting of trained immunity. Nat Rev Drug Discov *18*, 553-566. 10.1038/s41573-
1435 019-0025-4.
1436 Nakamura, T., Sakata, R., Ueno, T., Sata, M., and Ueno, H. (2000). Inhibition of transforming
1437 growth factor beta prevents progression of liver fibrosis and enhances hepatocyte regeneration
1438 in dimethylnitrosamine-treated rats. Hepatology *32*, 247-255. 10.1053/jhep.2000.9109.
1439 Nalio Ramos, R., Missolo-Koussou, Y., Gerber-Ferder, Y., Bromley, C.P., Bugatti, M., Nunez,
1440 N.G., Tosello Boari, J., Richer, W., Menger, L., Denizeau, J., et al. (2022). Tissue-resident
1441 FOLR2(+) macrophages associate with CD8(+) T cell infiltration in human breast cancer. Cell
1442 *185*, 1189-1207 e1125. 10.1016/j.cell.2022.02.021.
1443 Nguyen-Lefebvre, A.T., Ajith, A., Portik-Dobos, V., Horuzsko, D.D., Arbab, A.S., Dzutsev,
1444 A., Sadek, R., Trinchieri, G., and Horuzsko, A. (2018). The innate immune receptor TREM-1
1445 promotes liver injury and fibrosis. J Clin Invest *128*, 4870-4883. 10.1172/JCI98156.
1446 Peltier, A., Seban, R.D., Buvat, I., Bidard, F.C., and Mechta-Grigoriou, F. (2022). Fibroblast
1447 heterogeneity in solid tumors: From single cell analysis to whole-body imaging. Semin Cancer
1448 Biol. 10.1016/j.semcancer.2022.04.008.
1449 Pfister, D., Nunez, N.G., Pinyol, R., Govaere, O., Pinter, M., Szydlowska, M., Gupta, R., Qiu,
1450 M., Deczkowska, A., Weiner, A., et al. (2021). NASH limits anti-tumour surveillance in
1451 immunotherapy-treated HCC. Nature *592*, 450-456. 10.1038/s41586-021-03362-0.
1452 Pietras, E.M., Mirantes-Barbeito, C., Fong, S., Loeffler, D., Kovtonyuk, L.V., Zhang, S.,
1453 Lakshminarasimhan, R., Chin, C.P., Techner, J.M., Will, B., et al. (2016). Chronic interleukin-
1454 1 exposure drives haematopoietic stem cells towards precocious myeloid differentiation at the
1455 expense of self-renewal. Nat Cell Biol *18*, 607-618. 10.1038/ncb3346.
1456 Pizzolato, G., Kaminski, H., Tosolini, M., Franchini, D.M., Pont, F., Martins, F., Valle, C.,
1457 Labourdette, D., Cadot, S., Quillet-Mary, A., et al. (2019). Single-cell RNA sequencing unveils
1458 the shared and the distinct cytotoxic hallmarks of human TCRVdelta1 and TCRVdelta2
1459 gammadelta T lymphocytes. Proc Natl Acad Sci U S A *116*, 11906-11915.
1460 10.1073/pnas.1818488116.
1461 Qi, J., Sun, H., Zhang, Y., Wang, Z., Xun, Z., Li, Z., Ding, X., Bao, R., Hong, L., Jia, W., et al.
1462 (2022). Single-cell and spatial analysis reveal interaction of FAP(+) fibroblasts and SPP1(+)
1463 macrophages in colorectal cancer. Nat Commun *13*, 1742. 10.1038/s41467-022-29366-6.
1464 Roulot, D., Sevcsik, A.M., Coste, T., Strosberg, A.D., and Marullo, S. (1999). Role of
1465 transforming growth factor beta type II receptor in hepatic fibrosis: studies of human chronic
1466 hepatitis C and experimental fibrosis in rats. Hepatology *29*, 1730-1738.
1467 10.1002/hep.510290622.
1468 Sadik, A., Somarribas Patterson, L.F., Ozturk, S., Mohapatra, S.R., Panitz, V., Secker, P.F.,
1469 Pfander, P., Loth, S., Salem, H., Prentzell, M.T., et al. (2020). IL4I1 Is a Metabolic Immune
1470 Checkpoint that Activates the AHR and Promotes Tumor Progression. Cell *182*, 1252-1270
1471 e1234. 10.1016/j.cell.2020.07.038.
1472 Sharma, A., Seow, J.J.W., Dutertre, C.A., Pai, R., Bleriot, C., Mishra, A., Wong, R.M.M.,
1473 Singh, G.S.N., Sudhagar, S., Khalilnezhad, S., et al. (2020). Onco-fetal Reprogramming of
1474 Endothelial Cells Drives Immunosuppressive Macrophages in Hepatocellular Carcinoma. Cell
1475 *183*, 377-394 e321. 10.1016/j.cell.2020.08.040.

1476 Shen, Z.T., and Sigalov, A.B. (2017). Rationally designed ligand-independent peptide
1477 inhibitors of TREM-1 ameliorate collagen-induced arthritis. J Cell Mol Med *21*, 2524-2534.
1478 10.1111/jcmm.13173.
1479 Sica, A., Guarneri, V., and Gennari, A. (2019). Myelopoiesis, metabolism and therapy: a crucial
1480 crossroads in cancer progression. Cell Stress *3*, 284-294. 10.15698/cst2019.09.197.
1481 Sohn, B.H., Shim, J.J., Kim, S.B., Jang, K.Y., Kim, S.M., Kim, J.H., Hwang, J.E., Jang, H.J.,
1482 Lee, H.S., Kim, S.C., et al. (2016). Inactivation of Hippo Pathway Is Significantly Associated
1483 with Poor Prognosis in Hepatocellular Carcinoma. Clin Cancer Res *22*, 1256-1264.
1484 10.1158/1078-0432.CCR-15-1447.
1485 Song, G., Shi, Y., Zhang, M., Goswami, S., Afridi, S., Meng, L., Ma, J., Chen, Y., Lin, Y.,
1486 Zhang, J., et al. (2020). Global immune characterization of HBV/HCV-related hepatocellular
1487 carcinoma identifies macrophage and T-cell subsets associated with disease progression. Cell
1488 Discov *6*, 90. 10.1038/s41421-020-00214-5.
1489 Steen, C.B., Liu, C.L., Alizadeh, A.A., and Newman, A.M. (2020). Profiling Cell Type
1490 Abundance and Expression in Bulk Tissues with CIBERSORTx. Methods Mol Biol *2117*, 135-
1491 157. 10.1007/978-1-0716-0301-7_7.
1492 Sun, Y., Wu, L., Zhong, Y., Zhou, K., Hou, Y., Wang, Z., Zhang, Z., Xie, J., Wang, C., Chen,
1493 D., et al. (2021). Single-cell landscape of the ecosystem in early-relapse hepatocellular
1494 carcinoma. Cell *184*, 404-421 e416. 10.1016/j.cell.2020.11.041.
1495 Taieb, J., Chaput, N., Menard, C., Apetoh, L., Ullrich, E., Bonmort, M., Pequignot, M., Casares,
1496 N., Terme, M., Flament, C., et al. (2006). A novel dendritic cell subset involved in tumor
1497 immunosurveillance. Nat Med *12*, 214-219. 10.1038/nm1356.
1498 Teschendorff, A.E., and Enver, T. (2017). Single-cell entropy for accurate estimation of
1499 differentiation potency from a cell's transcriptome. Nat Commun *8*, 15599.
1500 10.1038/ncomms15599.
1501 Teschendorff, A.E., Maity, A.K., Hu, X., Weiyan, C., and Lechner, M. (2021). Ultra-fast
1502 scalable estimation of single-cell differentiation potency from scRNA-Seq data. Bioinformatics
1503 *37*, 1528-1534. 10.1093/bioinformatics/btaa987.
1504 Theurich, S., Tsaousidou, E., Hanssen, R., Lempradl, A.M., Mauer, J., Timper, K., Schilbach,
1505 K., Folz-Donahue, K., Heilinger, C., Sexl, V., et al. (2017). IL-6/Stat3-Dependent Induction of
1506 a Distinct, Obesity-Associated NK Cell Subpopulation Deteriorates Energy and Glucose
1507 Homeostasis. Cell Metab *26*, 171-184 e176. 10.1016/j.cmet.2017.05.018.
1508 Travaglini, K.J., Nabhan, A.N., Penland, L., Sinha, R., Gillich, A., Sit, R.V., Chang, S., Conley,
1509 S.D., Mori, Y., Seita, J., et al. (2020). A molecular cell atlas of the human lung from single-cell
1510 RNA sequencing. Nature *587*, 619-625. 10.1038/s41586-020-2922-4.
1511 Tsukuma, H., Hiyama, T., Tanaka, S., Nakao, M., Yabuuchi, T., Kitamura, T., Nakanishi, K.,
1512 Fujimoto, I., Inoue, A., Yamazaki, H., and et al. (1993). Risk factors for hepatocellular
1513 carcinoma among patients with chronic liver disease. N Engl J Med *328*, 1797-1801.
1514 10.1056/NEJM199306243282501.
1515 Veglia, F., Sanseviero, E., and Gabrilovich, D.I. (2021). Myeloid-derived suppressor cells in
1516 the era of increasing myeloid cell diversity. Nat Rev Immunol *21*, 485-498. 10.1038/s41577-
1517 020-00490-y.
1518 Veglia, F., Tyurin, V.A., Blasi, M., De Leo, A., Kossenkov, A.V., Donthireddy, L., To, T.K.J.,
1519 Schug, Z., Basu, S., Wang, F., et al. (2019). Fatty acid transport protein 2 reprograms
1520 neutrophils in cancer. Nature *569*, 73-78. 10.1038/s41586-019-1118-2.
1521 Villani, A.C., Satija, R., Reynolds, G., Sarkizova, S., Shekhar, K., Fletcher, J., Griesbeck, M.,
1522 Butler, A., Zheng, S., Lazo, S., et al. (2017). Single-cell RNA-seq reveals new types of human
1523 blood dendritic cells, monocytes, and progenitors. Science *356*. 10.1126/science.aah4573.

1524 Vosshenrich, C.A., Lesjean-Pottier, S., Hasan, M., Richard-Le Goff, O., Corcuff, E.,
1525 Mandelboim, O., and Di Santo, J.P. (2007). CD11cloB220+ interferon-producing killer
1526 dendritic cells are activated natural killer cells. J Exp Med *204*, 2569-2578.
1527 10.1084/jem.20071451.
1528 Weinreb, C., Rodriguez-Fraticelli, A., Camargo, F.D., and Klein, A.M. (2020). Lineage tracing
1529 on transcriptional landscapes links state to fate during differentiation. Science *367*.
1530 10.1126/science.aaw3381.
1531 Wu, J., Li, J., Salcedo, R., Mivechi, N.F., Trinchieri, G., and Horuzsko, A. (2012). The
1532 proinflammatory myeloid cell receptor TREM-1 controls Kupffer cell activation and
1533 development of hepatocellular carcinoma. Cancer Res *72*, 3977-3986. 10.1158/0008-
1534 5472.CAN-12-0938.
1535 Wu, Q., Zhou, W., Yin, S., Zhou, Y., Chen, T., Qian, J., Su, R., Hong, L., Lu, H., Zhang, F., et
1536 al. (2019). Blocking Triggering Receptor Expressed on Myeloid Cells-1-Positive Tumor-
1537 Associated Macrophages Induced by Hypoxia Reverses Immunosuppression and Anti-
1538 Programmed Cell Death Ligand 1 Resistance in Liver Cancer. Hepatology *70*, 198-214.
1539 10.1002/hep.30593.
1540 Zhang, Q., He, Y., Luo, N., Patel, S.J., Han, Y., Gao, R., Modak, M., Carotta, S., Haslinger, C.,
1541 Kind, D., et al. (2019). Landscape and Dynamics of Single Immune Cells in Hepatocellular
1542 Carcinoma. Cell *179*, 829-845 e820. 10.1016/j.cell.2019.10.003.
1543 Zheng, C., Zheng, L., Yoo, J.K., Guo, H., Zhang, Y., Guo, X., Kang, B., Hu, R., Huang, J.Y.,
1544 Zhang, Q., et al. (2017). Landscape of Infiltrating T Cells in Liver Cancer Revealed by Single-
1545 Cell Sequencing. Cell *169*, 1342-1356 e1316. 10.1016/j.cell.2017.05.035.
1546

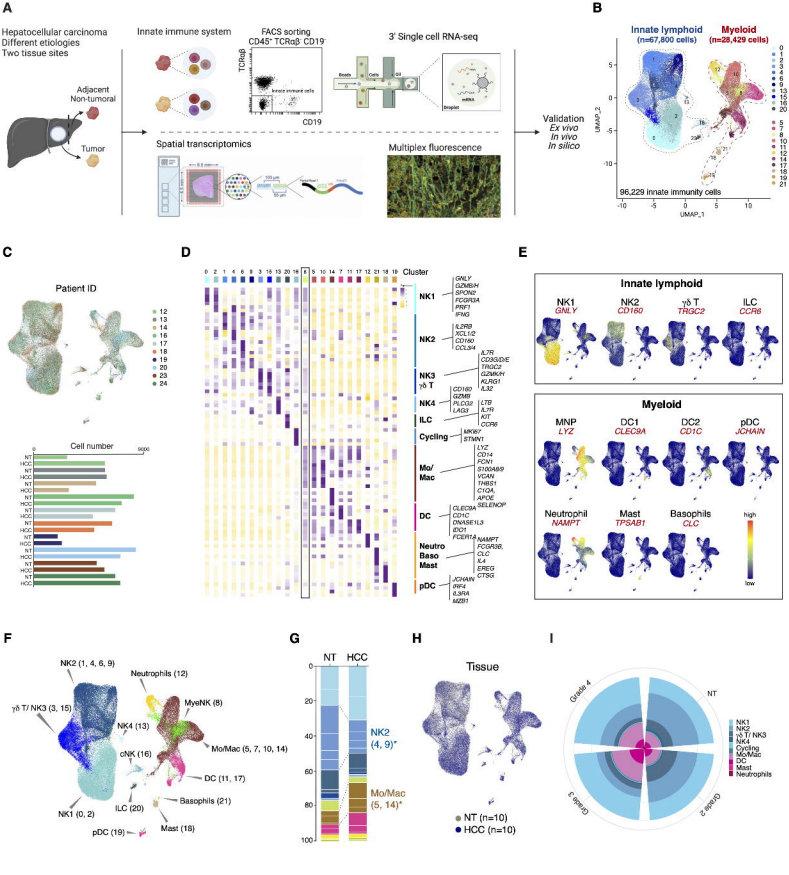
A
Hepatocellular carcinoma
Different etiologies
Two tissue sites
Adjacent Non-tumoral
Tumor
Innate immune system
FACS sorting
CD45+ TCRαβ- CD19-
TCRαβ
CD19
Innate immune cells
3' Single cell RNA-seq
Beads
Cells
Droplet
mRNA
Spatial transcriptomics
Multiplex fluorescence
Validation
Ex vivo
In vivo
In silico
B
Innate lymphoid (n=67,800 cells)
Myeloid (n=28,429 cells)
96,229 innate immunity cells
UMAP_1
UMAP_2
C
Patient ID
Cell number
D
Cluster
NK1
NK2
γδ T
NK3
NK4
ILC
Cycling
Mo/Mac
DC
Neutro
Baso
Mast
pDC
E
Innate lymphoid
NK1 GNLY
NK2 CD160
γδ T TRGC2
ILC CCR6
Myeloid
MNP LYZ
DC1 CLEC9A
DC2 CD1C
pDC JCHAIN
Neutrophil NAMPT
Mast TPSAB1
Basophils CLC
high
low
F
NK2 (1, 4, 6, 9)
Neutrophils (12)
γδ T/ NK3 (3, 15)
MyeNK (8)
NK4 (13)
Mo/Mac (5, 7, 10, 14)
cNK (16)
DC (11, 17)
Basophils (21)
ILC (20)
NK1 (0, 2)
Mast (18)
pDC (19)
G
NT
HCC
NK2 (4, 9)*
Mo/Mac (5, 14)*
H
Tissue
NT (n=10)
HCC (n=10)
I
Grade 4
Grade 3
Grade 2
NT
NK1
NK2
γδ T/ NK3
NK4
Cycling
Mo/Mac
DC
Mast
Neutrophils

Figure 1

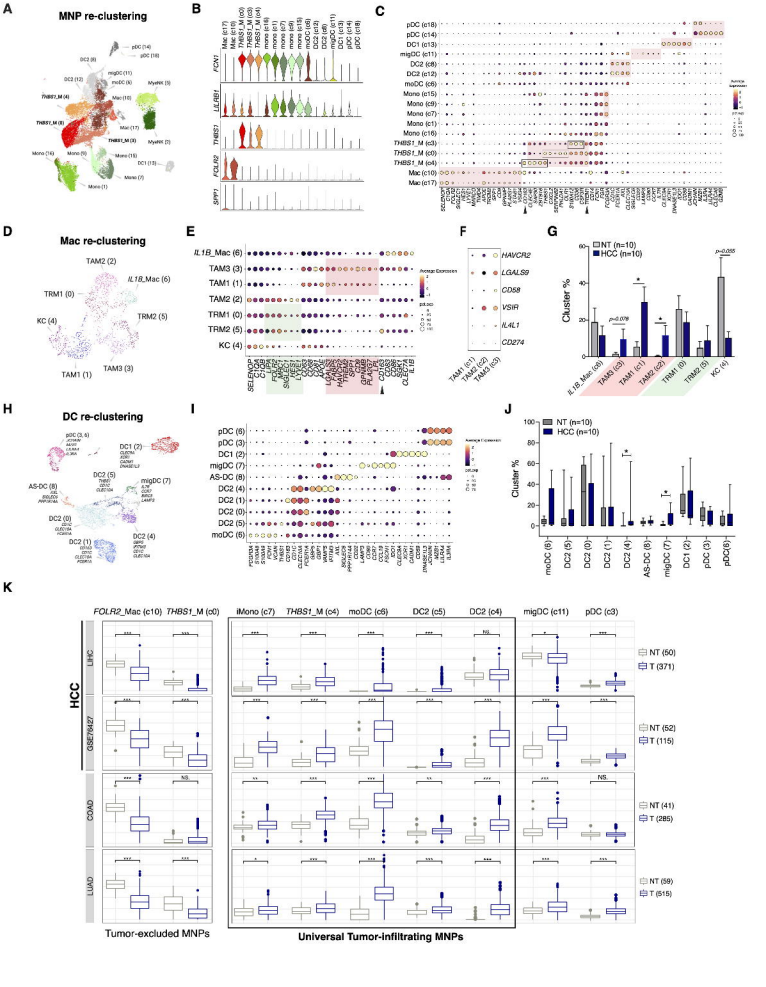
A
MNP re-clustering
B
C
D
Mac re-clustering
E
F
G
NT (n=10)
HCC (n=10)
Cluster %
H
DC re-clustering
I
J
K
HCC
LIHC
GSE76427
COAD
LUAD
Tumor-excluded MNPs
Universal Tumor-infiltrating MNPs
NT (50)
T (371)
NT (52)
T (115)
NT (41)
T (285)
NT (59)
T (515)

Figure 2

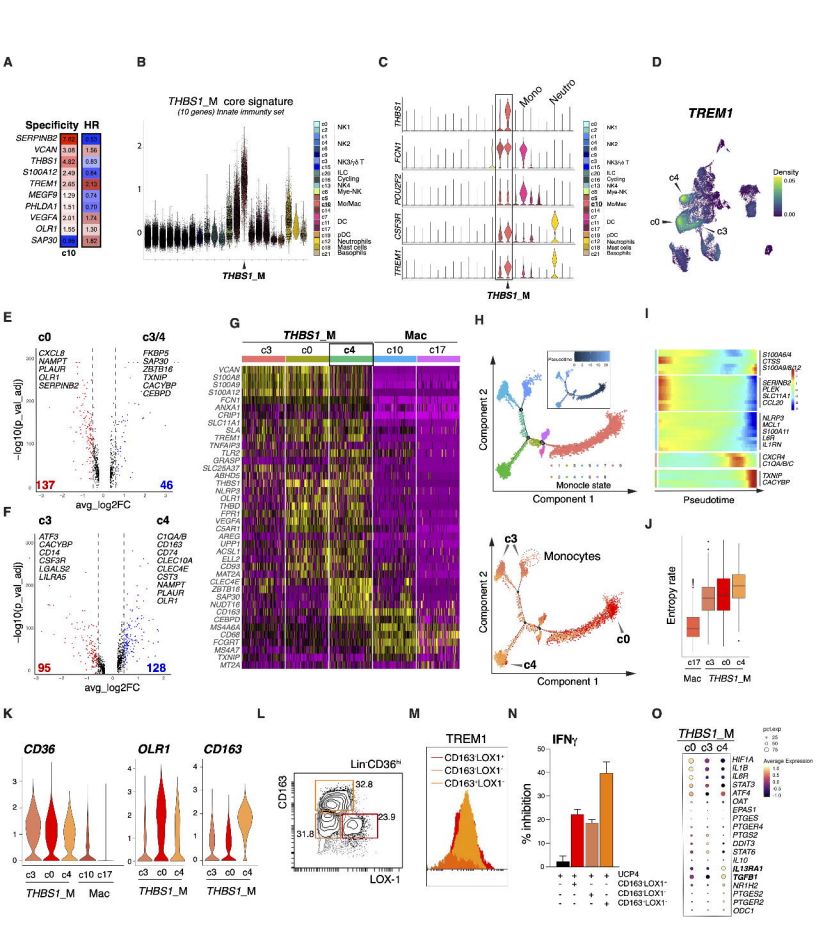
A
Specificity
HR
SERPINB2 5.08 2.34
VCAN 3.08 1.56
THBS1 4.62 0.83
S100A12 2.49 0.64
TREM1 2.65 2.12
MEGF9 1.29 0.74
PHLDA1 1.91 0.70
VEGFA 2.01 1.74
OLR1 1.55 1.30
SAP30 1.18 1.82
c10
B
THBS1_M core signature
(10 genes) innate immunity set
NK1
NK2
NKγδ T
ILC
Cycling
NK4
Myel-NK
MoMac
DC
pDC
Neutrophils
Mast cells
Basophils
THBS1_M
C
Mono
Neutro
THBS1
FCN1
PDUFB2
CSF3R
TREM1
THBS1_M
D
TREM1
Density
c4
c0
c3
E
c0
c3/4
CXCL8
NAMPT
PLAUR
OLR1
SERPINB2
FKBP5
SAP30
ZBTB16
TXNIP
CACYBP
CEBPD
137
46
avg_log2FC
-log10(p_val_adj)
F
c3
c4
ATF3
CACYBP
CD14
CSF3R
LGALS2
LILRA5
C1QA/B
CD163
CD74
CLEC10A
CLECAE
CST3
NAMPT
PLAUR
OLR1
95
128
avg_log2FC
-log10(p_val_adj)
G
THBS1_M
Mac
c3
c0
c4
c10
c17
VCAN
S100A8
S100A9
S100A12
FCN1
ANXA1
CRIP1
SLC11A1
SLA
TREM1
TNFAIP2
TLR2
SLC25A37
ABHD5
THBS1
NLRP3
OLR1
THBD
FPR1
VEGFA
CSAR1
AREG
UPP1
ACSL1
ELL2
CD93
MAT2A
CLEC4E
ZBTB16
SAP30
NUDT16
CD163
CEBPD
MS4A6A
CD68
FCGR1
MS4A7
TXNIP
MT2A
H
Pseudotime
Component 2
Component 1
Monocle state
c3
Monocytes
c0
c4
Component 2
Component 1
I
S100A6/4
CTSS
S100A9/8/12
SERPINB2
PLEK
SLC11A1
CCL20
NLRP3
MCL1
S100A11
L6R
IL1RN
CXCR4
C1QA/B/C
TXNIP
CACYBP
Pseudotime
J
Entropy rate
c17
c3
c0
c4
Mac
THBS1_M
K
CD36
OLR1
CD163
c3
c0
c4
c10
c17
THBS1_M
Mac
L
CD163
Lin⁻CD36ʰⁱ
32.8
23.9
31.8
LOX-1
M
TREM1
CD163⁺LOX1⁺
CD163⁺LOX1⁺
CD163⁻LOX1⁺
N
IFNγ
% inhibition
UCP4
CD163⁺LOX1⁺
CD163⁺LOX1⁺
CD163⁻LOX1⁺
O
THBS1_M
c0
c3
c4
HIF1A
IL1B
IL6R
STAT3
ATF4
CMT
EPAS1
PTGES
PTGER4
PTGS2
DDIT3
STAT6
IL10
IL13RA1
TGFB1
NR1H2
PTGES2
PTGER2
ODC1
Average Expression

Figure 3

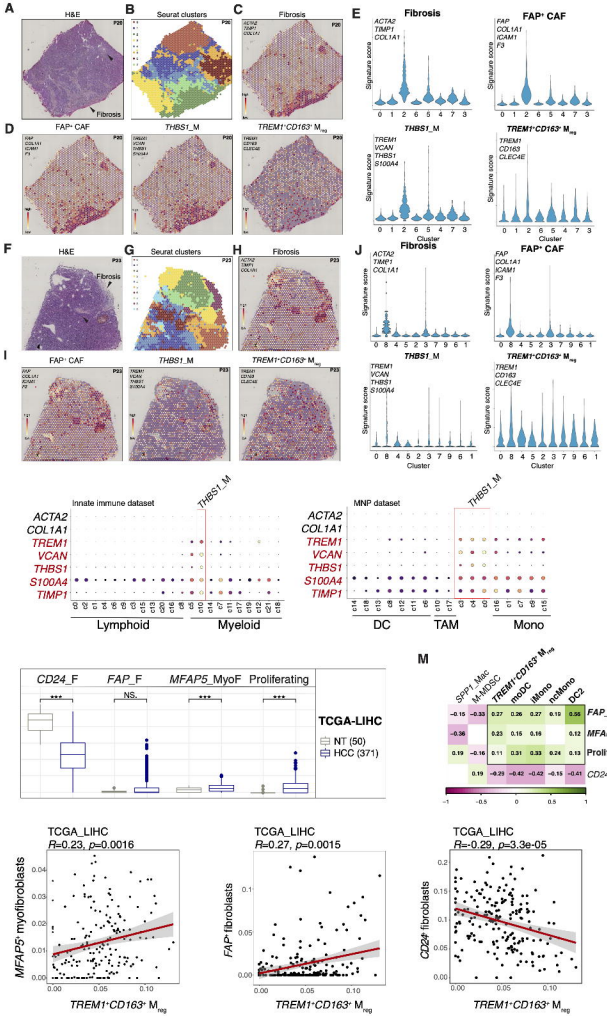
A
H&E
Fibrosis
B
Seurat clusters
C
Fibrosis
D
FAP+ CAF
THBS1_M
TREM1+CD163+ Mreg
E
Fibrosis
FAP+ CAF
THBS1_M
TREM1+CD163+ Mreg
Signature score
Cluster
F
H&E
Fibrosis
G
Seurat clusters
H
Fibrosis
I
FAP+ CAF
THBS1_M
TREM1+CD163+ Mreg
J
Fibrosis
FAP+ CAF
THBS1_M
TREM1+CD163+ Mreg
Signature score
Cluster
K
Innate immune dataset
MNP dataset
THBS1_M
ACTA2
COL1A1
TREM1
VCAN
THBS1
S100A4
TIMP1
Lymphoid
Myeloid
DC
TAM
Mono
L
CD24_F
FAP_F
MFAP5_MyoF
Proliferating
NS.
TCGA-LIHC
NT (50)
HCC (371)
M
SPP1_Mac
M-MDSC
TREM1+CD163+ Mreg
mnDC
iMono
ncMono
DC2
FAP_F
MFAP5_MyoF
Proliferating
CD24_F
N
TCGA_LIHC
R=0.23, p=0.0016
MFAP5+ myofibroblasts
TREM1+CD163+ Mreg
TCGA_LIHC
R=0.27, p=0.0015
FAP+ fibroblasts
TREM1+CD163+ Mreg
TCGA_LIHC
R=-0.29, p=3.3e-05
CD24+ fibroblasts
TREM1+CD163+ Mreg

Figure 4

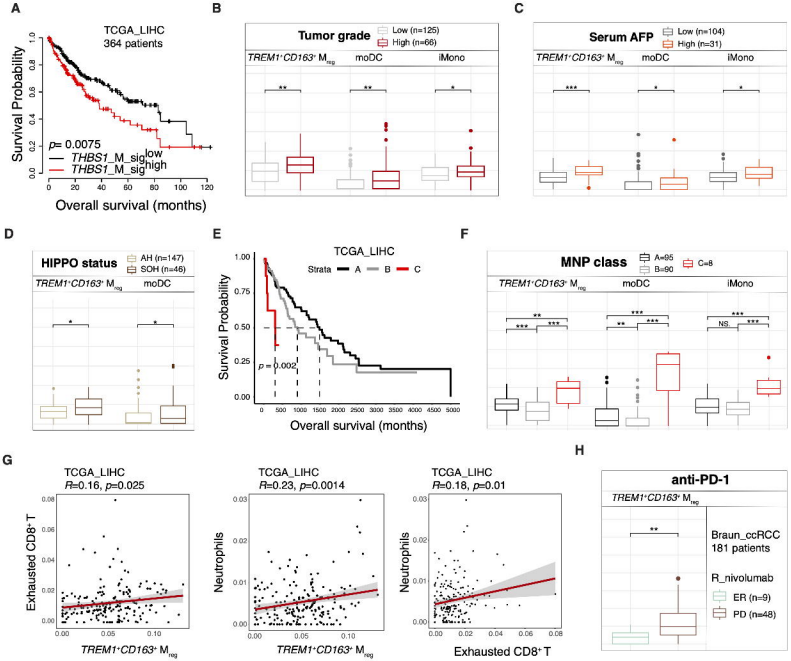
A
TCGA_LIHC
364 patients
Survival Probability
p= 0.0075
THBS1_M_sig low
THBS1_M_sig high
Overall survival (months)
B
Tumor grade
Low (n=125)
High (n=66)
TREM1+CD163+ Mreg
moDC
iMono
C
Serum AFP
Low (n=104)
High (n=31)
D
HIPPO status
AH (n=147)
SOH (n=46)
E
TCGA_LIHC
Strata A B C
p = 0.002
Overall survival (months)
F
MNP class
A=95
B=90
C=8
G
TCGA_LIHC
R=0.16, p=0.025
Exhausted CD8+ T
R=0.23, p=0.0014
Neutrophils
R=0.18, p=0.01
H
anti-PD-1
Braun_ccRCC
181 patients
R_nivolumab
ER (n=9)
PD (n=48)

Figure 5

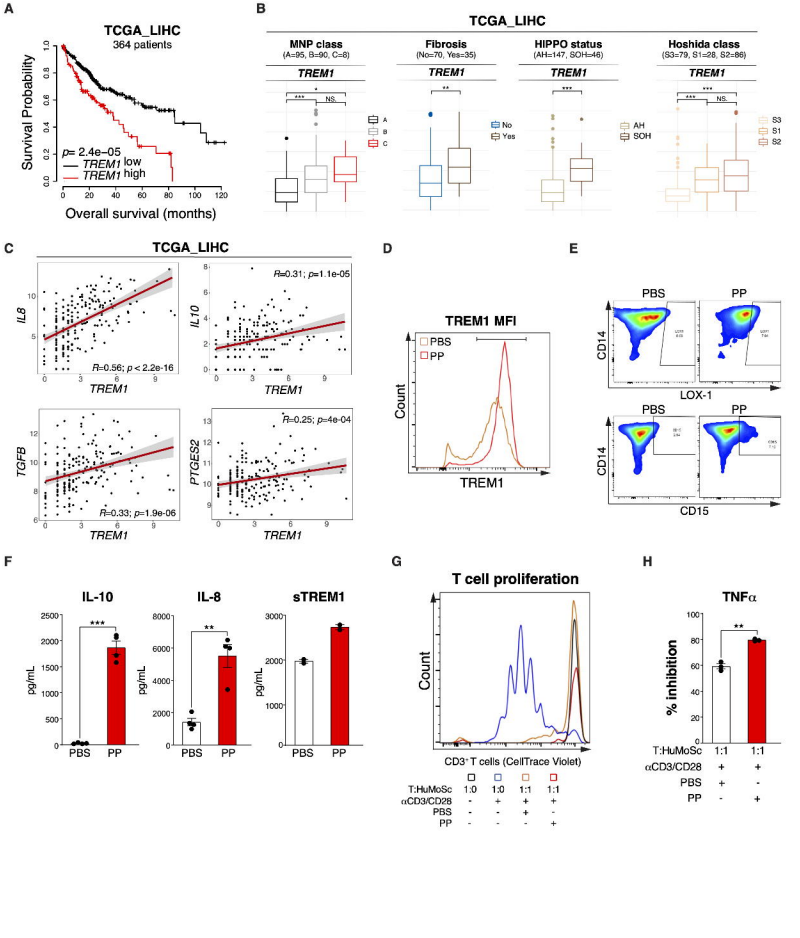
A
TCGA_LIHC
364 patients
Survival Probability
p= 2.4e-05
TREM1 low
TREM1 high
Overall survival (months)
B
TCGA_LIHC
MNP class
(A=95, B=90, C=8)
Fibrosis
(No=70, Yes=35)
HIPPO status
(AH=147, SOH=46)
Hoshida class
(S3=79, S1=28, S2=86)
TREM1
NS.
A
B
C
No
Yes
AH
SOH
S3
S1
S2
C
TCGA_LIHC
IL8
IL10
TGFB
PTGES2
TREM1
R=0.56; p < 2.2e-16
R=0.31; p=1.1e-05
R=0.33; p=1.9e-06
R=0.25; p=4e-04
D
TREM1 MFI
PBS
PP
Count
TREM1
E
PBS
PP
CD14
LOX-1
CD15
F
IL-10
IL-8
sTREM1
pg/mL
PBS
PP
G
T cell proliferation
Count
CD3+ T cells (CellTrace Violet)
T:HuMoSc 1:0 1:0 1:1 1:1
αCD3/CD28 - + + +
PBS - - + -
PP - - - +
H
TNFα
% inhibition
T:HuMoSc 1:1 1:1
αCD3/CD28 + +
PBS + -
PP - +

Figure 6

A

Patient ID	Clinical information							Recovery cell number (15.000 input cells)	
	Age	Sex	Grade	Treatment (chemoembolization)	NASH (n=3/10)	Cirrhosis (n=3/10)	Virus (HCV, n=3/10)	Non-tumoral liver	Tumor
12	68	F	3	yes	no	yes	yes	2387	4957
13	63	M	3	no	yes	no	no	5058	5111
14	62	M	3	yes	no	no	no	4564	1953
16	85	M	2	no	no	no	yes	7288	6396
17	78	M	2	no	no	no	no	6019	4363
18	78	M	2	yes	yes	yes	no	5102	4239
19	60	M	3	non	no	no	no	1710	1836
20	74	M	4	no	no	no	no	7398	6212
23	70	M	4	no	yes	yes	no	4691	5281
24	69	M	3	no	no	no	yes	5592	6072
n=10				n=3/10	n=3/10	n=3/10	n=3/10	49809	46420

B

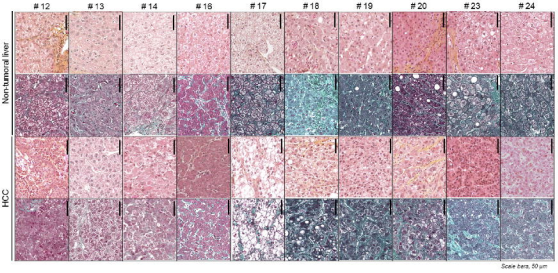

C

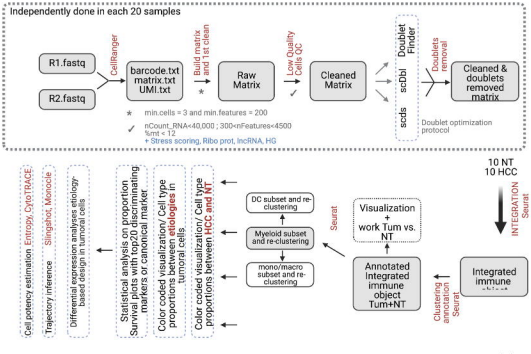

Figure S1

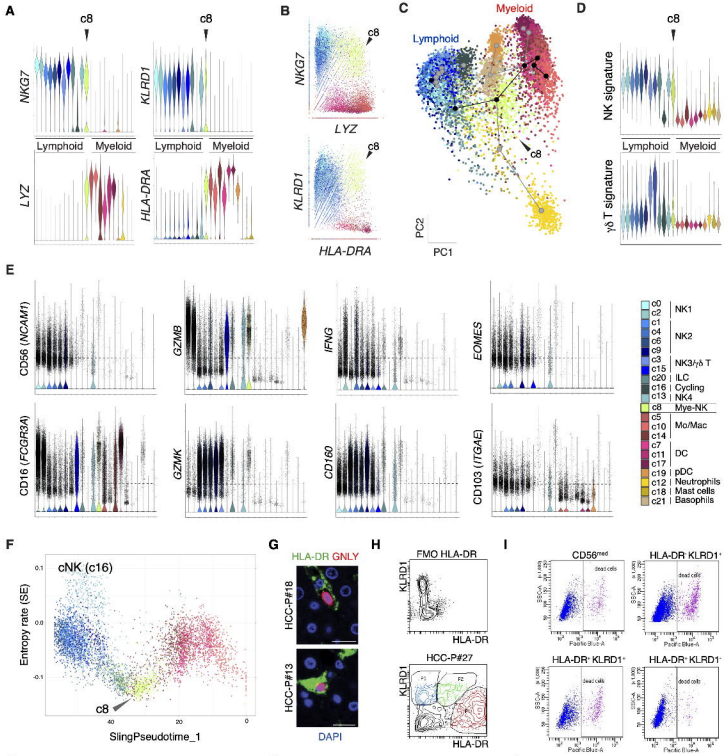
A
c8
NKG7
KLRD1
LYZ
HLA-DRA
Lymphoid
Myeloid
B
NKG7
LYZ
KLRD1
HLA-DRA
c8
C
Lymphoid
Myeloid
c8
PC2
PC1
D
NK signature
γδ T signature
E
CD56 (NCAM1)
GZMB
IFNG
EOMES
CD16 (FCGR3A)
GZMK
CD160
CD103 (ITGAE)
c0 c2 c1 c4 c6 c9 NK1
NK2
c3 c15 NK3/γδ T
c20 iLC
c16 Cycling
c13 NK4
c8 Mye-NK
c5 c10 c14 Mo/Mac
c7 c11 c17 DC
c19 pDC
c12 Neutrophils
c18 Mast cells
c21 Basophils
F
cNK (c16)
Entropy rate (SE)
c8
SlingPseudotime_1
G
HLA-DR GNLY
HCC-P#18
HCC-P#13
DAPI
H
FMO HLA-DR
KLRD1
HLA-DR
HCC-P#27
P1
P2
I
CD56med
HLA-DR- KLRD1+
HLA-DR+ KLRD1+
HLA-DR+ KLRD1-
dead cells
SSC-A
Pacific Blue-A
J
- IL-2/IL-15
+ IL-2/IL-15
Cytotoxicity (%)
-
CD56med
KLRD1+ HLA-DR-
KLRD1+ HLA-DR+
KLRD1- HLA-DR+
K
Tissue
NT (n=10)
HCC (n=10)
Cluster %
MyeNK (c5)
MyeNK
c5
c2
L
Obesity (NT)
no
yes
NASH (NT)
MyeNK (c5)

Figure S2

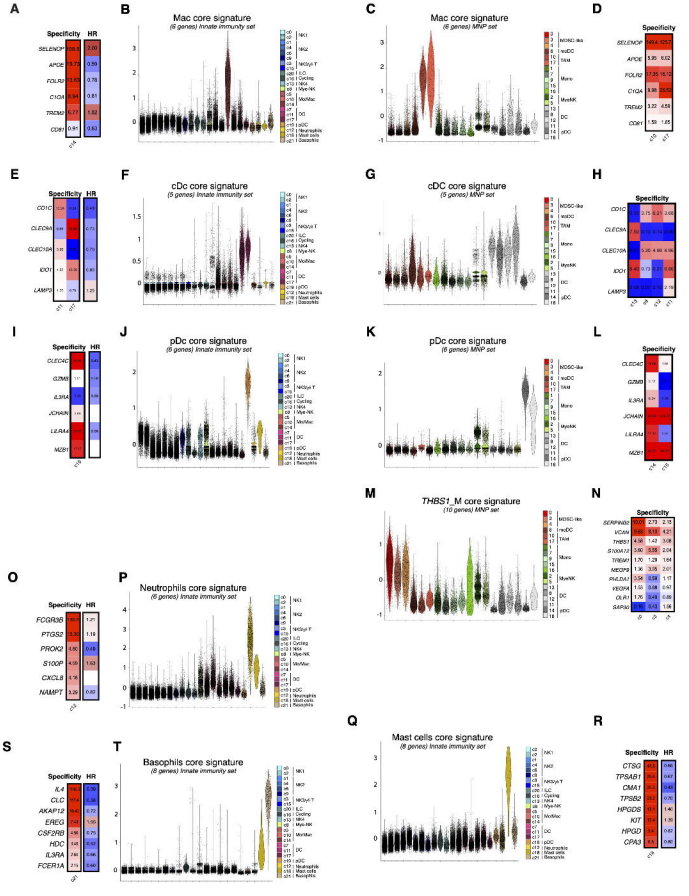
A
Specificity
HR
SELENOP
APOE
FOLR2
C1QA
TREM2
CD81
B
Mac core signature
(8 genes) Innate immunity set
C
Mac core signature
(8 genes) MNP set
D
Specificity
E
Specificity
HR
CD1C
CLECD4A
CLEC10A
IDO1
LAMP3
F
cDc core signature
(8 genes) Innate immunity set
G
cDc core signature
(8 genes) MNP set
H
Specificity
I
Specificity
HR
CLEC4C
GZMB
IL3RA
JCHAIN
LILRA4
MZB1
J
pDc core signature
(8 genes) Innate immunity set
K
pDc core signature
(8 genes) MNP set
L
Specificity
M
THBS1_M core signature
(10 genes) MNP set
N
Specificity
SERPINB2
VCAN
THBS1
S100A12
TREM1
MEGF9
PHLDA1
VEGFA
OLR1
SAP30
O
Specificity
HR
FCGR3B
PTGS2
PROK2
S100P
CXCL8
NAMPT
P
Neutrophils core signature
(8 genes) Innate immunity set
Q
Mast cells core signature
(8 genes) Innate immunity set
R
Specificity
HR
CTSG
TPSAB1
CMA1
TPSB2
HPGDS
KIT
HPGD
CPA3
S
Specificity
HR
IL4
CLC
AKAP12
EREG
CSF2RB
HDC
IL3RA
FCER1A
T
Basophils core signature
(8 genes) Innate immunity set

Figure S3

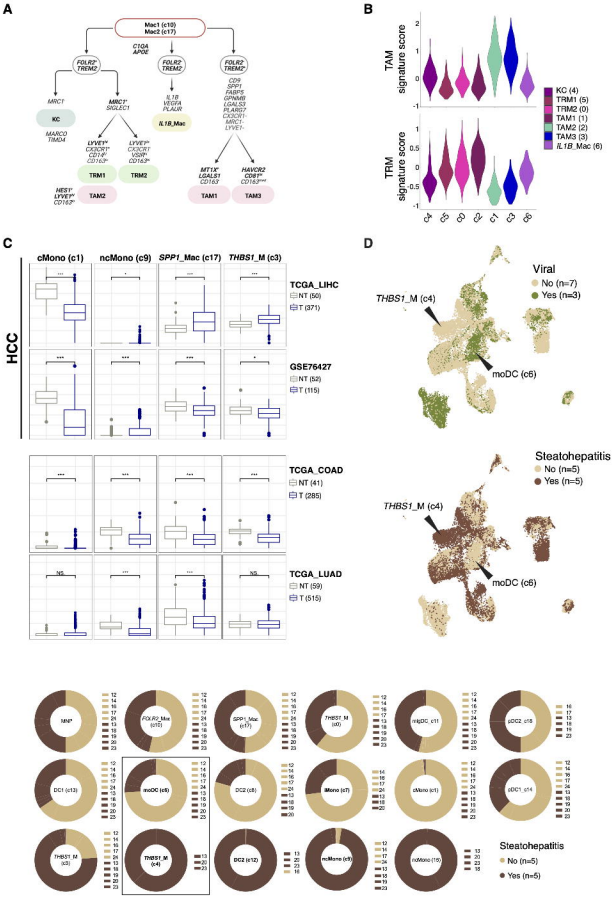
A
Mac1 (c10)
Mac2 (c17)
C1QA
APOE
FOLR2
TREM2
FOLR2
TREM2
FOLR2
TREM2
MRC1
MRC1
SIGLEC1
IL1B
VEGFA
PLAUR
CD9
SPP1
FABP5
GPNMB
LGALS3
PLAUR2
CXCR1
MRC1
LYVE1
KC
MARCO
TIMD4
IL1B_Mac
LYVE1
CXCR1
CD14
CD163
LYVE1
CXCR1
CD14
CD163
TRM1
TRM2
MT1X
LGALS1
CD163
HAVCR2
CD81
CD163
HES1
LYVE1
CD163
TAM2
TAM1
TAM3
B
TAM signature score
TRM signature score
KC (4)
TRM1 (5)
TRM2 (0)
TAM1 (1)
TAM2 (2)
TAM3 (3)
IL1B_Mac (6)
c4
c5
c0
c2
c1
c3
c6
C
cMono (c1)
ncMono (c9)
SPP1_Mac (c17)
THBS1_M (c3)
HCC
TCGA_LIHC
NT (50)
T (371)
GSE76427
NT (52)
T (115)
TCGA_COAD
NT (41)
T (285)
TCGA_LUAD
NT (59)
T (515)
D
Viral
No (n=7)
Yes (n=3)
THBS1_M (c4)
moDC (c6)
Steatohepatitis
No (n=5)
Yes (n=5)
THBS1_M (c4)
moDC (c6)
E
MNP
FOLR2_Mac (c12)
SPP1_Mac (c17)
THBS1_M (c0)
HBDC_c11
cDC2_c15
DC1 (c13)
moDC (c6)
DC2 (c5)
iMono (c7)
cMono (c1)
cDC1_c14
THBS1_M (c3)
THBS1_M (c4)
DC2 (c12)
ncMono (c9)
ncMono (15)
Steatohepatitis
No (n=5)
Yes (n=5)

Figure S4

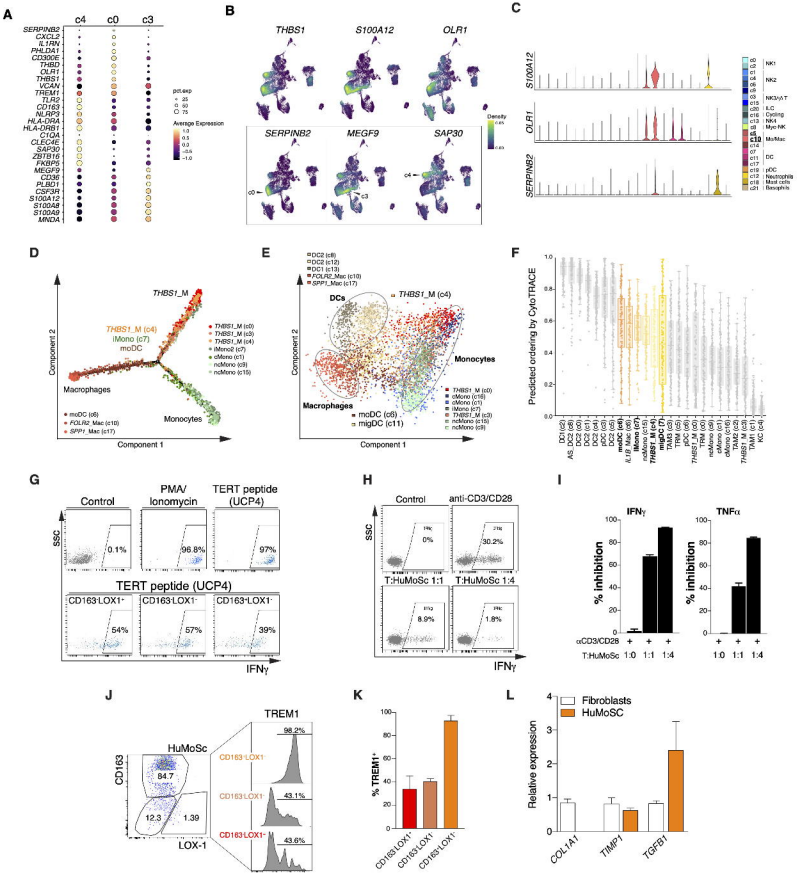
A
c4
c0
c3
SERPINB2
CXCL2
IL1RN
PHLDA1
CD300E
THBD
OLR1
THBS1
VCAN
TREM1
TLR2
CD163
NLRP3
HLA-DRA
HLA-DRB1
C1QA
CLEC4E
SAP30
ZBTB16
FKBP5
MEGF9
CD36
PLBD1
CSF3R
S100A12
S100A8
S100A9
MNDA
pct.exp
Average Expression
B
THBS1
S100A12
OLR1
SERPINB2
MEGF9
SAP30
Density
C
S100A12
OLR1
SERPINB2
NK1
NK2
NK3/γΔT
ILC
Cycling
NK4
Mye NK
Mo/Mac
DC
pDC
Neutrophils
Mast cells
Basophils
D
THBS1_M
THBS1_M (c4)
iMono (c7)
moDC
Macrophages
Monocytes
Component 1
Component 2
E
DC2 (c8)
DC2 (c12)
DC1 (c13)
FOLR2_Mac (c10)
SPP1_Mac (c17)
DCs
THBS1_M (c4)
Monocytes
Macrophages
moDC (c6)
migDC (c11)
Component 1
Component 2
F
Predicted ordering by CytoTRACE
G
Control
PMA/ Ionomycin
TERT peptide (UCP4)
SSC
0.1%
96.8%
97%
TERT peptide (UCP4)
CD163-LOX1+
CD163-LOX1-
CD163+LOX1-
54%
57%
39%
IFNγ
H
Control
anti-CD3/CD28
SSC
0%
30.2%
T:HuMoSc 1:1
T:HuMoSc 1:4
8.9%
1.8%
IFNγ
I
IFNγ
TNFα
% inhibition
αCD3/CD28
T:HuMoSc
1:0
1:1
1:4
J
TREM1
HuMoSc
CD163
84.7
12.3
1.39
LOX-1
CD163-LOX1+
CD163-LOX1-
98.2%
43.1%
43.6%
K
% TREM1+
CD163-LOX1+
CD163-LOX1-
CD163+LOX1-
L
Fibroblasts
HuMoSC
Relative expression
COL1A1
TIMP1
TGFB1

Figure S5

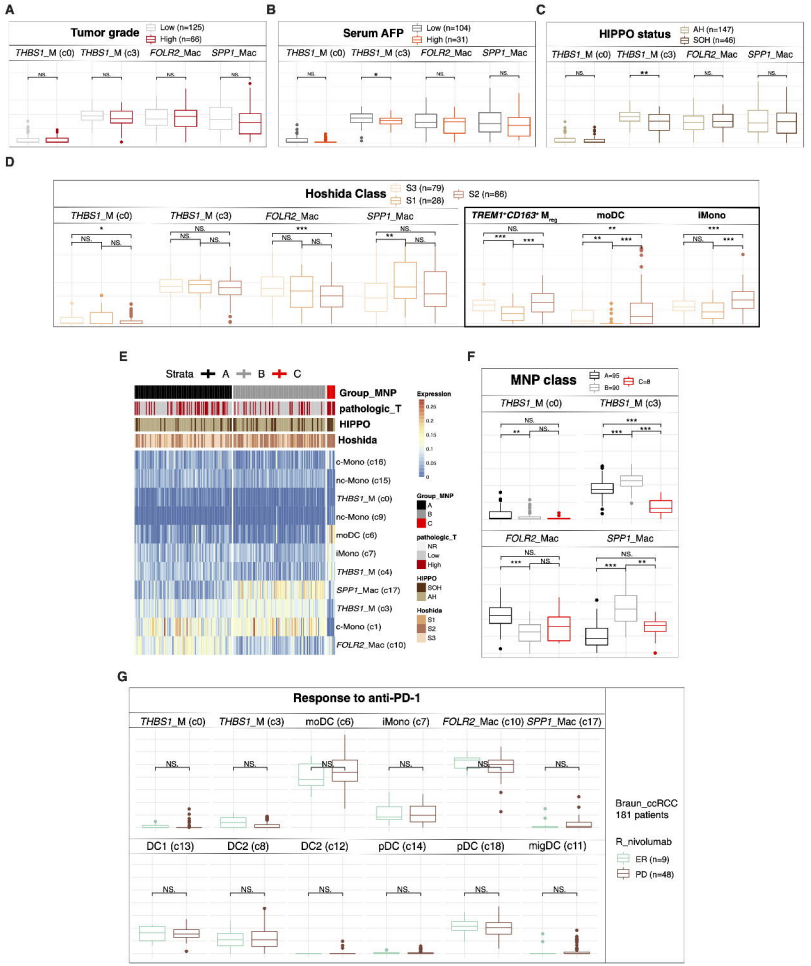
A
Tumor grade
Low (n=125)
High (n=66)
THBS1_M (c0)
THBS1_M (c3)
FOLR2_Mac
SPP1_Mac
B
Serum AFP
Low (n=104)
High (n=31)
C
HIPPO status
AH (n=147)
SOH (n=46)
D
Hoshida Class
S3 (n=79)
S1 (n=28)
S2 (n=86)
TREM1+CD163+ Mreg
moDC
iMono
E
Strata A B C
Group_MNP
pathologic_T
HIPPO
Hoshida
c-Mono (c16)
nc-Mono (c15)
THBS1_M (c0)
nc-Mono (c9)
moDC (c6)
iMono (c7)
THBS1_M (c4)
SPP1_Mac (c17)
THBS1_M (c3)
c-Mono (c1)
FOLR2_Mac (c10)
Expression
Group_MNP
pathologic_T
NR
Low
High
HIPPO
SOH
AH
Hoshida
S1
S2
S3
F
MNP class
A=95
B=90
C=8
G
Response to anti-PD-1
DC1 (c13)
DC2 (c8)
DC2 (c12)
pDC (c14)
pDC (c18)
migDC (c11)
Braun_ccRCC
181 patients
R_nivolumab
ER (n=9)
PD (n=48)

Figure S6

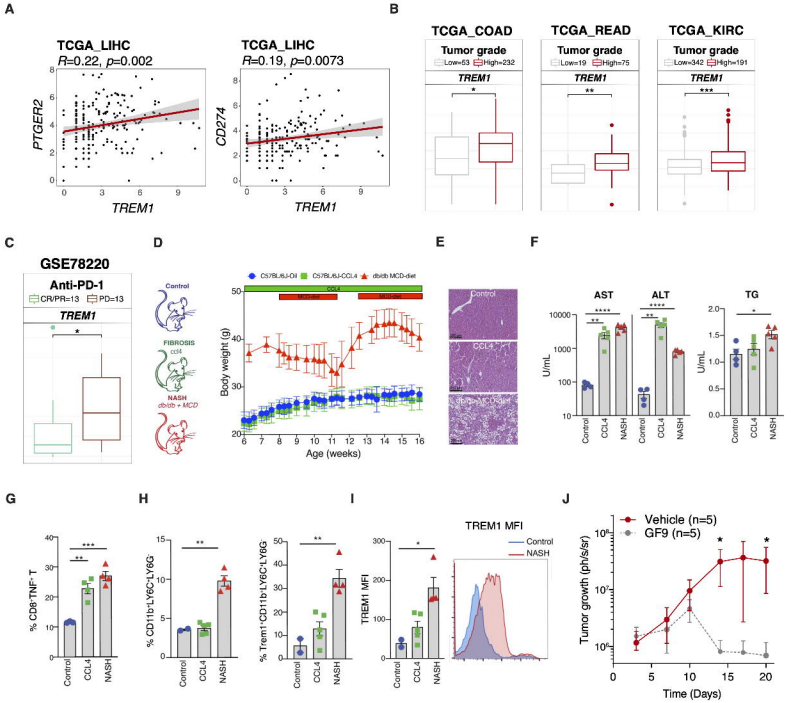
A
TCGA_LIHC
R=0.22, p=0.002
PTGER2
TREM1
TCGA_LIHC
R=0.19, p=0.0073
CD274
TREM1
B
TCGA_COAD
Tumor grade
Low=53
High=232
TREM1
TCGA_READ
Tumor grade
Low=19
High=75
TREM1
TCGA_KIRC
Tumor grade
Low=342
High=191
TREM1
C
GSE78220
Anti-PD-1
CR/PR=13
PD=13
TREM1
D
Control
FIBROSIS
CCl4
NASH
db/db + MCD
C57BL/6J-Oil
C57BL/6J-CCL4
db/db MCD-diet
CCl4
Recovery
Body weight (g)
Age (weeks)
E
Control
CCL4
db/db MCD-diet
F
AST
ALT
TG
U/mL
Control
CCL4
NASH
G
% CD8+TNF+ T
Control
CCL4
NASH
H
% CD11b+LY6C+LY6G
Control
CCL4
NASH
I
% Trem1+CD11b+LY6C+LY6G
TREM1 MFI
Control
NASH
J
Vehicle (n=5)
GF9 (n=5)
Tumor growth (ph/s/sr)
Time (Days)

Figure S7